Flow Analysis of Rimer Alco North America's Refuge One

by

Sarwesh Mali

A Thesis submitted to the Faculty of Graduate Studies of

The University of Manitoba

in partial fulfilment of the requirements of the degree of

MASTER OF SCIENCE

Department of Mechanical Engineering

University of Manitoba

Winnipeg

ABSTRACT

This study is part of a multi-disciplinary research effort to better understand, document and optimize the operation of Rimer Alco North America's Refuge One for the global mining industry. In this thesis, an experimental and numerical study of turbulent flow inside a Refuge One is undertaken to understand the flow characteristics through a Refuge One hopper, compare the predictive performance of five different turbulence models and optimize the flow through the Refuge One hopper to enhance its performance. The experimental study is performed using a particle image velocimetry technique for two Reynolds numbers 53,000 and 23,000, respectively. The numerical study is performed by solving the Reynolds-Averaged Navier-Stokes equations together with $k-\varepsilon$, RNG $k-\varepsilon$, $k-\omega$, $k-\omega$ based SST and Reynolds stress turbulence models using the commercial CFD code CFX 15.0. Flow optimization is performed for hoppers by choosing different hopper height and wall shape configurations and their performances are evaluated.

ACKNOWLEDGEMENT

I would like to express my sincere gratitude to my advisor Dr. Mark F. Tachie for his invaluable support and guidance during this research. I would also like to thank Professor Vern Campbell for his support and guidance.

The financial support provided by MITACS, Rimer Alco North America and NSERC Engage Grant is greatly appreciated.

I am also grateful to Mr. Ali Nematollahi, Ebenezer E. Essel and Blaise Oscar Bwabwa for their support. I would also like to acknowledge the technical support from Mr. Paul Krueger.

TABLE OF CONTENTS

LIST OF FIGURES

LIST OF TABLES

NOMENCLATURE

English

C_p	pressure coefficient
C_f	skin friction coefficient
d	hopper exit diameter
d_p	seeding particle diameter
g	acceleration due to gravity
h	hopper height
k	turbulent kinetic energy
k_c	pressure loss coefficient
P	plane of measurement
P_k	production term
Q	flow rate
Re	Reynolds number
Re_D	Reynolds number based on upstream contraction diameter
Re_d	Reynolds number based on downstream contraction diameter
Re_m	Reynolds number based on mesh length of grid

Re_Θ	Reynolds number based on momentum thickness
U	mean streamwise velocity
U_{max}	maximum streamwise velocity at hopper exit
U_{exit}	centerline streamwise velocity at hopper exit
$-uv$	Reynolds shear stress
u	streamwise turbulence intensity
u^2	streamwise Reynolds normal stress
V	wall-normal mean velocity
v	wall-normal turbulence intensity
v^2	wall-normal Reynolds normal stress
x	streamwise distance
y	wall-normal distance
y^+	non dimensional distance from the wall

Greek

ε	turbulent dissipation rate
θ	momentum thickness
ΔH	head loss

Δs	local displacement vector
Δt	laser time delay
∇P	pressure drop
τ_r	response time
ρ_p	seeding particle density
ρ_f	fluid density
$\dot{m}$	mass flow
μ	fluid dynamic viscosity
μ_t	turbulent eddy viscosity
v_s	settling velocity
ω	specific turbulence dissipation
Ω	vorticity

Acronyms

3D	three-dimensional
CAD	computer aided design

CCD	charged coupled device
CFD	computational fluid dynamics
DMADV	define, measure, analyze, design and verify
DNS	direct numerical simulation
FPG	favorable pressure gradient
FVM	finite volume method
IA	interrogation area
LDA	laser Doppler anemometry
LES	large eddy simulation
Nd:YAG	neodymium Yttrium Aluminium Garnet
PIV	particle image velocimetry
RANS	Reynolds averaged Navier-Stokes
RNG	re-normalization group
RSM	Reynolds stress model
SST	shear stress transport

1 CHAPTER: INTRODUCTION

1.1 Background and Motivation

Mining accidents are accidents that occur during the process of mining minerals. Over the past century, mining accidents have resulted in the deaths of thousands of mine workers around the world mostly in coal and hard rock mining industries. International Labor Organisation estimates that just one percent of the world's labour workforce is engaged in mining, while the industry accounts for five percent of on the job fatalities from mining accidents.

One of history's worst mining accidents took place in the Benxihu Colliery coal mine on April 26, 1942 in China where mine fires claimed the lives of 1,549 miners. Since then many countries have enforced strict regulations and enforcement standards to ensure safety of miners. Developed countries like the U.S. and Canada have acknowledged the risks from previous mining accidents that these mining accidents need not necessarily become human tragedies. The International Labor Organisation's recent statistics show a significant decline in the rate of fatal injuries in the Canadian mining sector between 1998 and 2010, falling from 47.1 per 100,000 employees to 9.3 per 100,000 employees, respectively (Marshall, 2013). One of the most recent mining accidents in Canada happened on April 6th, 2015 at Vale Canada mine in northern Manitoba, where an underground fire broke out with 39 miners trapped inside. A safety procedure was initiated and the miners were sent into multiple mine refuge stations to await rescue. Fortunately, within the next day mine rescue teams had accounted for all the 39 men and they were secured on surface. Despite this positive outcome, mining accidents seem too inevitable because they are dramatic and all too frequent reminders of the dangerous and uncertain conditions in which miners work.

Most underground mines are equipped with a ventilation system that draws fresh air into the mine to dilute and remove potentially dangerous gases and dust. However, the safety of miners can be threatened if the ventilation system fails to adequately ventilate the mine. In such circumstances, the miners trapped in underground mines without breathable air can find themselves at great risk of substantial injury or even death. To overcome this, mine refuge stations are built in underground mines. The purpose of mine refuge stations is to keep miners safe in case of mining accidents. Mine refuge stations comprise a chamber sized and shaped for multiple miner's occupancy. In such chambers, oxygen supply is adapted to ensure supply of oxygen and carbon-dioxide reduction system is used to remove carbon dioxide in the chamber. These oxygen supply and carbon dioxide removal systems are operable in the mine refuge stations even without an electrical power source.

Rimer Alco North America (RANA) is one of the global leaders in manufacturing and supply of mine refuge systems for the international mining industry. RANA supplies mine refuge systems to numerous international mining companies such as Vale, Goldcorp, HudBay, Glencore, Agnico Eagle Mines Limited and AuRico Gold. RANA has developed a mine safety device known as the Refuge One over 20 years ago. The development of Refuge One came about with the realization after a mining accident in Canada that it was not only important to have mine refuge stations but to have breathable air in the stations for a minimal period of time for mine rescue to reach the occupants. In 1995, RANA developed the award-winning Refuge One breathable air center and the mobile refuge chamber known as the Tommyknocker. The Refuge One is recognised both nationally and internationally. In September 1995, Refuge One received the top honour in the international field of applied research, the U.S.'s research and development award (R and D 100) and again in October 1996, Refuge One received

Canada's OHS innovative product award of excellence in occupational health and safety (Rimer Alco North America, 2010).

The Refuge One provides breathable air to both permanent refuge chambers and mobile units, such as Tommyknockers. It is an independent system located inside mine refuge stations. The Refuge One is used to supplement oxygen flow at controlled rates and remove carbon dioxide from the air in enclosed space to maintain breathable air environment during mine emergency. To replenish oxygen consumed by the occupants, oxygen from high-pressure cylinders is injected at metered rate depending on the number of occupants and carbon dioxide is removed by passing the air in the rescue chamber through carbon dioxide scrubbers by means of blowers in the Refuge One. Some advantages of Refuge One are as follows: compressed air pipelines are eliminated as the air in the rescue chamber is processed by the unit, it does not require an external power source, it is portable and can be easily moved from one rescue chamber to another and it does not need any additional volume of space as the size of the refuge stations need to only accommodate the Refuge One and number of occupants.

The major components of Refuge One are as follows: hopper, blower, chemical scrubber, battery, battery charger, chemical bed and oxygen valve. Figure 1.1 shows a photo of Refuge One.

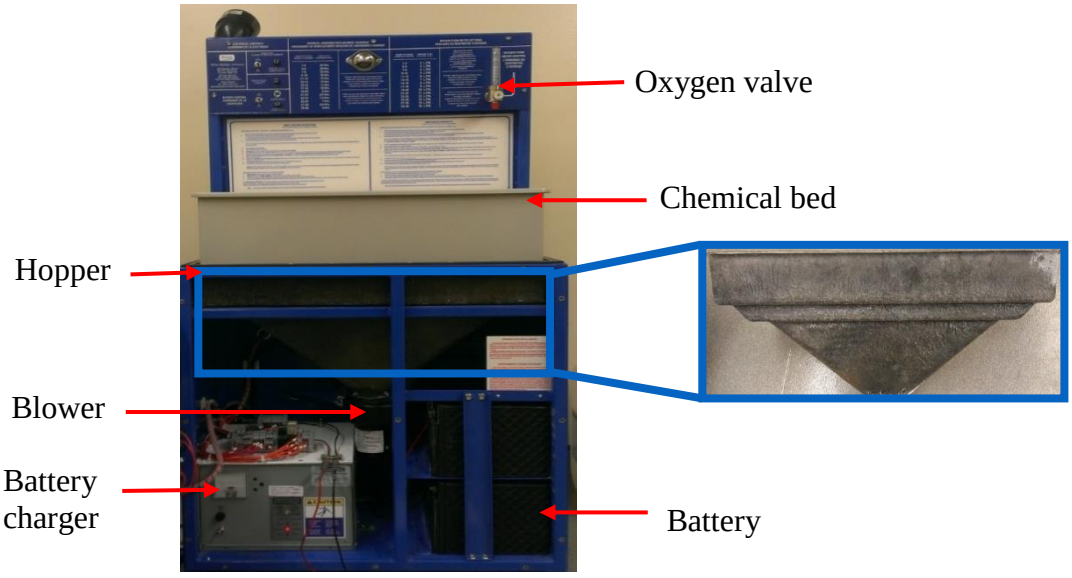

Figure 1.1: A photo of Refuge One showing its main components with inset showing zoomed picture of hopper.

Since the Refuge One was introduced 20 years ago, there has been little change in its design. Demand for RANA's Refuge One is projected to increase in the near future because of the growing mining industry. Therefore, there is a need to redesign the unit for efficient manufacturability. There are also changed industry safety requirements specifying that the unit be designed in such a way that the unit's battery life is extended to 96 hours from the current 36 hours. In addition, RANA has also received feedback from their customer base suggesting that the Refuge One be redesigned to incorporate new product features deemed important to their customers. Some of the important product features requested by their customers are: redundant blowers, carbon monoxide scrubbers, battery indicators and pre-packaged chemical cartridges.

In order to meet the industry and customer demand, RANA initiated a collaborative research project with the University of Manitoba to better understand, document and optimize the operation of the Refuge One. The overall objective of this collaborative project is to provide a final design prototype of the Refuge One to RANA using design for six sigma define, measure, analyze, design and verify (DMADV) methodology. This

multidisciplinary project involves optimal manufacturing process based on DMADV methodology and also analysis of fluid flow through the Refuge One. However, only the second part of this collaborative research which involves the fluid flow analysis and optimization through the Refuge One hopper will be presented in this study.

One approach to perform fluid flow analysis through the Refuge One is to use an experimental method. Although experiments remain a powerful methodology in the study of fluid flows, design of optimal fluid engineering devices by experimental means alone is a daunting task partly because of the huge cost and time required to setup and perform refined measurements. An alternative approach is to use computational fluid dynamics (CFD) based numerical methods. CFD techniques are relatively less expensive and even complex fluid flow geometries can be explored more easily and quickly than is possible in physical experiments. Reynolds Averaged Navier-Stokes (RANS) technique is one of the popular CFD methods. RANS technique requires less computational effort than other numerical techniques such as direct numerical simulations and large eddy simulations, and is the method used for calculating most engineering fluid flows. However, the accuracy of RANS models depends on the choice of turbulence models. RANS models, if selected and applied properly with suitable turbulence models, offer engineers a highly attractive balance between computing resources and accuracy required for most industrial applications. Therefore, in this study it is proposed to employ a balanced approach which involves comprehensive experimental study and numerical analysis of fluid flow in the Refuge One hopper. The experiments will provide insight into the flow field and this knowledge base will guide the selection of appropriate numerical models. The benchmark experimental dataset will be used to validate the numerical results. Once the appropriate model is identified,

it will be used to perform optimization analysis on a wide range of hopper geometries with specific flow conditions to identify the optimal design.

1.2 Objectives

The main objectives of this study are as follows: (a) to perform experimental study of flow characteristics through the Refuge One hopper (b) to compare the experimental results with those of several turbulence models using RANS, in order to assess their predictive performance, and (c) to perform optimization of flow through the Refuge One hopper after selecting an appropriate turbulence model.

The first objective is achieved by using a particle image velocimetry (PIV) system to conduct detailed whole-field velocity measurements of the fluid flow through Refuge One hopper. This experimental study will provide benchmark dataset to validate the numerical models. The second objective is achieved by using a commercial CFD code ANSYS® CFX 15.0 to numerically analyze fluid flow through the Refuge One hopper using different turbulence models available in CFX. The numerical results will be validated with the experimental dataset to select the most appropriate turbulence model that can accurately predict the experimental results. The third objective is achieved by numerical simulation of fluid flow through different hopper geometries using ANSYS® CFX 15.0 to identify the optimum design.

1.3 Layout of the thesis

A comprehensive literature review is presented in chapter 2. The literature review summarizes the most relevant experimental and numerical works on fluid flow through contractions. The experimental methodology used in the present study is described in chapter 3, and the numerical modelling is discussed in chapter 4. Results and discussions of the experimental and numerical works are presented in chapter 5.

Numerical optimization of hopper geometry is also presented in chapter 5, while conclusions and recommendations for future work are presented in Chapter 6.

2 CHAPTER: LITERATURE REVIEW

The goal of this chapter is to summarize some of the relevant experimental and numerical studies from the extensive literature on fluid flow through contractions, followed by a summary of studies on optimization of contraction geometry.

2.1 Background

A hopper is a mechanical device with a converging section attached to a pipe. They are used to collect and facilitate the flow of substances entering through their larger opening and exiting through the attached pipe with a smaller opening. Depending on specific applications, hoppers may have pyramidal, conical or square taper surfaces connecting the fluid entry and exit sections. In Refuge One, conical hoppers are used to collect the flow passing through the chemical bed which has a rectangular cross section and accelerate the flow as it enters the blower connected at the circular exit of the hopper. There are two experiments that have been conducted in the past to study the efficiency of Refuge One (Grenier et al., 1993; Gardiner et al., 1994). The purpose of their experiments was to test the ability of Refuge One to provide volunteers with breathable air during a 24 hour period in the absence of compressed air. The experiments were simulated in a real life emergency situation. The major conclusions were that the Refuge One was able to keep the carbon dioxide at a safe level which is below 2,300 ppm, and oxygen level within an acceptable range varying between 19.5% and 20.9%. This provided the volunteers with a breathable air environment for the entire 24 hour period. Furthermore, the volunteers also recommended that the unit was easy to operate and the instruction manuals were clear. However, the fluid flow characteristics through the Refuge One hoppers have not been investigated in detail to assess their effects on head losses. The efficiency of Refuge One can be improved significantly and its battery life increased by performing detailed experimental and numerical analysis to

understand how the hopper geometry and fluid flow conditions affect the losses through the Refuge One hoppers. This will help in selecting the optimal Refuge One hopper geometry under the most efficient flow conditions.

2.2 Introduction

Flows through contractions are an active area of research because of their diverse engineering applications such as heating, ventilation and air conditioning systems, polymer processes and nozzle designs. They are also used as pipe fittings to connect pipes with different diameters. Contractions are also important components of aerodynamic and hydrodynamic tunnels as they are used just before the test section to reduce turbulence levels as flow acceleration achieved in the contraction produces more uniform velocity profile at the inlet of the test section. However, for mixing applications higher turbulence levels through contraction may be more desirable.

Gradual contractions have cross sectional area that slowly decreases, and this slowly increases the velocity of the flow as opposed to sudden contractions, where the flow velocity increases abruptly causing flow recirculation at the corners. Gradual contractions have Tapered or curved surfaces joining the fluid entry and exit locations. As shown in Figure 1.1, hoppers are gradual contractions with Tapered surfaces having industrial significance. There have been many studies on fluid flows through gradual contractions with curved surfaces as these type of contractions are generally used in wind and water tunnels. In addition, due to the simple geometry of sudden contractions, they have been regarded as a benchmark problem in fluid dynamics and there have been numerous studies investigating abrupt contraction fluid flows (Vrentas and Duda, 1973; Bullen, et al., 1987; Hussain, 1990; Bullen, et al., 1996; Sanchez, et al., 2010; Ray, et al., 2012). In contrast, limited research has been undertaken to understand fluid flows

through contractions such as a hopper which is a type of contraction with Tapered surfaces.

2.3 Previous works

2.3.1 Experimental studies

Over the years, extensive studies have been conducted to understand the flow characteristics through contractions. The availability of experimental data for fluid flows through contractions have both practical and theoretical importance. Practically, experimental data are needed to develop correlations in the design of contractions. Theoretically, data are needed to validate numerical simulations of fluid flows through contractions. Some of the pertinent experimental studies performed for fluid flows through contractions are summarized in Table 2.1. In Table 2.1, Re_D is the Reynolds number based on upstream contraction diameter, Re_d is the Reynolds number based on downstream contraction diameter and contraction ratio is defined as the ratio of inlet area to exit area of the contraction.

Most of the experimental studies on fluid flows through sudden contractions are focused on measurement of velocity field, vortex dynamics and pressure drop. Durst and Loy (1985), used laser Doppler anemometry (LDA) to investigate laminar flows through a sudden contraction and their work presented data on the size of recirculation bubble, reattachment length, velocity profiles and pressure losses through the contraction region. Khezzar and Whitelaw (1988) used LDA and provided measurements for velocity and wall static pressure characteristics in a sudden contraction for upstream Reynolds number of 40,000. They reported the presence of vena contractra and wall pressure drop through the contraction. Bullen et al. (1987) experimentally studied sudden contraction pressure losses for a range of upstream

Reynolds numbers from 40,000 to 200,000. They found that pressure coefficient is inversely proportional to Reynolds number. In a more recent study, Bullen et al. (1996) used LDA technique for an upstream Reynolds number of 153,800 and showed formation of vena contracta in the downstream of the contraction and the location of the reattachment point. Ozalp et al. (2007) performed experiments using a particle image velocimetry (PIV) technique and reported contours of streamwise and wall-normal mean velocities within the upstream of the contraction for upstream Reynolds numbers from 223 to 1,325. The most recent work on sudden contractions was performed by Sanchez et al. (2010). They used PIV technique to obtain velocity profiles in the streamwise and wall-normal direction along the upstream region of the contraction. They also studied flow patterns to observe the formation of vortex regions, and pressure coefficients were obtained for upstream Reynolds numbers from 17,000 to 40,000. Their results showed that the vortex size decreased as Reynolds number increased. The experimental results were compared to numerical results obtained using standard $k-\varepsilon$ turbulence model. It was reported that standard $k-\varepsilon$ model was able to predict the mean velocities and pressure coefficient reasonably well, however discrepancies in maximum velocities near the contraction were observed. Some relevant works in sudden contraction fluid flows dealing with non-Newtonian fluids (Boger, 1987; Fester, et al., 2008 and Sousa et al., 2011) and multiphase fluids (Jansen, 1966; Gnglielmini, et al., 1986; Schmidt and Friedel, 1977 and Roul and Dash, 2008) have also been reported.

The early studies on fluid flows through gradual contractions were initiated by researchers interested in wind tunnel designs. Uberoi (1956) investigated the effect of contraction on free stream turbulence using hot wire probes for contraction ratios of 4, 9 and 16. The results showed that the streamwise component of turbulence intensity

decreased and the wall-normal component increased as the flow passed through the contraction. Hussain and Ramjee (1976a) investigated the effects of four different axisymmetric shapes with contraction ratio of 11.1. They measured mean and turbulent velocity profiles before and after contraction using hot wire anemometers. They found that mean velocities and wall-normal turbulence intensities in the core region at the exit plane are unaffected by the contraction shape. In most of the measurements, the streamwise turbulence first decreased before increasing downstream of the contraction. In another study by Hussain and Ramjee (1976b), the effect of contraction ratio on free stream turbulence was investigated. They found that exit turbulence is independent of initial turbulence produced by grids placed upstream of the contraction. The streamwise turbulence intensity decreased through the contraction with increasing contraction ratio, the decrease being larger for higher contraction ratios. Prinos and Goulas (1993) investigated turbulent pipe flow with a gradual contraction using LDA and hot wires along the downstream and upstream of the contraction for upstream Reynolds numbers of 100,000 and 150,000. They found that there was a weak dependence of flow characteristics on Reynolds numbers investigated. The results were compared to standard $k-\varepsilon$ model and low Reynolds number $k-\varepsilon$ model of Launder and Sharma (1974). Both turbulence models reasonably predicted the mean velocities, however discrepancies were observed for turbulence kinetic energy. In a more recent study by Han et al. (2005), hot wires were used to measure turbulence statistics along the center line of the contraction. They reported that contraction reduced the streamwise components of turbulence and amplified the wall-normal components.

Table 2.1: Summary of the previous experimental studies

Author (s)	**Reynolds number (s)**	**Technique (s)**	**Contraction type**	**Contraction ratio (s)**	**Quantities measured**
Khezzar and Whitelaw (1988)	Re_D = 40,000	LDA	Sudden	2.5	U, V, u, v and C_p
Bullen et al. (1987)	Re_D = 40,000 - 200,000	-	Sudden	1.4, 1.9, 2.4, 3.3, 4.8 and 7.4	k_c
Bullen et al. (1996)	Re_D = 153, 800	LDA	Sudden	3	U, V, u, v, u^2, v^2 and k_c
Ozalp et al. (2007)	Re_D = 223, 336, 880 and 1,325	PIV	Sudden	16	U, V, Ω and u
Sanchez et al. (2010)	Re_D = 17,000 - 40,000	PIV	Sudden	3.8	U, V, ∇P and K_c
Uberoi (1956)	Re_m = 6,150 and 12,300 (based on mesh length of grid)	Hotwire	Gradual	4, 9 and 16	U, V, u, v, u^2 and v^2
Hussain and Ramjee (1976a)	Re_d = 140,000	Hotwire	Gradual	11.1	U, u, v, u^2, v^2, δ^*, θ and H
Hussain and Ramjee (1976b)	Re_d = 73,000 - 140,000	Hotwire	Gradual	11, 22, 44.5, 64 and 100	U, u, v, u^2, v^2 and θ
Prinos and Goulas (1993)	Re_D = 100,000 - 150,000	LDA and hotwire	Gradual	4.1	U, u, v, u^2, v^2, C_p and C_f
Han et al. (2005)	Re = 3,400 (based on grid size)	Hotwire	Gradual	11.3	U, u, v, u^2 and v^2

2.3.2 Numerical studies

It is recognized that turbulent flows contain a wide range of length and time scales. Therefore, the accuracy of numerical simulation increases if it can resolve all the scales of turbulence in a fluid flow. Direct numerical simulation (DNS) is a numerical technique that solves the exact fluid flow equations without introducing a turbulence model. In DNS, the whole range of turbulent scales is resolved. However, this incurs a huge computational cost, and cannot compute complex geometries and high Reynolds number engineering fluid flows. The application of large eddy simulations (LES) which resolves the highly energetic large scales and models the small scales of turbulence is also limited to relatively simple geometries because LES also requires fine grids to resolve the small scales compared to Reynolds-averaged Navier-Stokes (RANS) technique (Celik, 2005). Thus, the most popular numerical approach in CFD for turbulent flows of engineering importance is the RANS technique owing to its less computational cost, robustness and reasonable predictive accuracy.

The ability to correctly predict turbulent flows for complex geometries easily and quickly has made RANS technique a valuable tool in the design of many fluid engineering systems. In addition, numerical simulation of engineering fluid flows can provide very detailed information about the performance of complex fluid engineering systems at a much lower cost in comparison to physical experiments. However, there are many factors influencing the predictive performance of numerical models. One of the critical factors that determines the predictive accuracy of numerical simulations is the selection of turbulence models. Therefore, considerable effort has been made in the development of turbulence models by many researchers (Hanjalic, 1994; Hwang and Jaw, 1998; Gatski and Rumsey, 2002; Leschziner, 2006). As indicated by Hanjalic (1994), the complexity of turbulence models vary from the simple algebraic models

through two-equation eddy-viscosity models to second moment closures. The two-equation models use eddy viscosity hypothesis which relates Reynolds stresses to the mean velocity gradients and turbulent viscosity. Turbulent viscosity is computed as the product of turbulent velocity scale and length scale as proposed by Prandtl and Kolmogorov and discussed in Pope (2000). By definition, two-equation models use two extra transport equations to represent the turbulent flow properties. Mostly, turbulent kinetic energy (k) is one of the transport variables and the second transport variable depends on the type of two equation model. The turbulent velocity scale is computed from, k, which is obtained from the solution of its transport equation. The turbulent length scale is computed from, k, and the second transport variable. The second moment closure differs from the two equation models because it solves all the independent components of the Reynolds stress tensor, and does not invoke the eddy viscosity concept. Detailed description of various turbulence models can be found in Wilcox (1994). Some of the pertinent numerical studies performed for fluid flows through contractions are summarized in Table 2.2, where the parameters $Re_{D,}$ Re_d, and contraction ratio have the same meaning as described earlier.

The standard $k-\varepsilon$ model proposed by Launder and Spalding (1974) has been extensively used for predicting fluid flows through gradual and sudden contractions because of its robustness, vast validation and reasonable accuracy. Hussain (1990) numerically simulated fluid flow through a sudden contraction for upstream Reynolds number of 153,800. He concluded that $k-\varepsilon$ model was able to reasonably predict the mean velocities; however, significant discrepancies were observed close to the wall downstream of the contraction. Sanchez et al. (2010) also used $k-\varepsilon$ model to predict fluid flow through a sudden contraction and concluded that this model was capable of reproducing the mean velocity with a reasonable accuracy. However, according to

Prinos and Goulas (1993), the $k-\varepsilon$ model with a standard wall function may have difficulty predicting skin friction values for gradual contraction flows accurately compared to turbulence models that have enhanced wall treatment capability. Unfortunately, there were no comparisons made with experimental data.

The Re-Normalization (RNG) $k-\varepsilon$ model developed by Yakhot et al. (1992) has also been used to predict fluid flows through contractions. In comparison to standard $k-\varepsilon$ model, the RNG $k-\varepsilon$ model takes into account the effect of small scale motions and low-Reynolds number effects. The RNG $k-\varepsilon$ model has been suggested to offer improved accuracy over standard $k-\varepsilon$ turbulence models for fluid flows with significant streamline curvature. Yassen and Abdelhamed (2015) simulated fluid flows through wind tunnel consisting of a gradual contraction using the RNG $k-\varepsilon$ model and obtained satisfactory agreement with the experimental data.

The $k-\omega$ model of Wilcox (1986) is more accurate and numerically stable in the near wall region than the standard $k-\varepsilon$ model. Ahmed and Eljack (2014) used $k-\omega$ model to analyze and optimize fluid flow through a three dimensional wind tunnel contraction. Also, Mathew (2006) used $k-\omega$ model to analyze fluid flow through a gradual contraction and found that the model was able to satisfactorily predict flow separation through the contraction.

The $k-\omega$ based shear stress transport (SST) model of Menter (1994) has also been widely used in predicting fluid flows through contractions because it combines the advantages of $k-\varepsilon$ and $k-\omega$ model to achieve an optimal model formulation for a wide range of flow conditions. Wexler (2014) used the $k-\omega$ based SST, Spalart-Allmaras, $k-\varepsilon$ and $k-\omega$ models to predict the velocity downstream of a gradual contraction. By comparing the numerical and experimental results, it was concluded

that all the four turbulence models satisfactorily predicted the mean features of the flow, however, $k-\omega$ based SST model had a better predictive performance. Many existing studies on fluid flow optimization through gradual contractions have used $k-\omega$ based SST model (Sargison et al., 2004; Clark, 2010; Bouriga et al., 2014; Abdelhamed et al., 2014).

Reynolds stress model (RSM) model developed by Launder et al. (1975) is a more sophisticated model that abandons the hypothesis of isotropic turbulence and solves the transport equations for the Reynolds stresses together with the equation for the dissipation rate. Although the complexity of RSM gives it a larger potential to cope with complex flows than two equation models, the accuracy of RSM is limited by the assumptions related to several terms in the transport equations which often is considered responsible for degrading the accuracy of numerical simulations predicted by RSM. Notwithstanding the complexity, RSM have been used to predict fluid flows through contractions. Mattos et al. (2003) used RSM model to predict the flow field through wind tunnel contractions. Yu et al. (2012) compared the predictive performances of $k-\varepsilon$, RNG $k-\varepsilon$, $k-\omega$, $k-\omega$ based SST and RSM models in the context of fluid flow through a nozzle which is a type of a gradual contraction. They showed that all the turbulence models satisfactorily predicted the mean velocities, however discrepancies were observed for turbulence quantities. Among all the turbulence models, $k-\omega$ based SST model and RSM reasonably predicted the turbulence statistics, however compared to experimental results only RSM model captured the peak value of the streamwise turbulent intensity near the wall.

Table 2.2: Summary of the previous numerical studies

Author (s)	**Reynolds number (s)**	**Numerical Model (s)**	**Contraction type**	**Contraction ratio (s)**
Hussain (1990)	Re_D= 153,800	$k-\varepsilon$	Sudden	3
Sanchez et al. (2010)	Re_D = 17,000 - 40,000	$k-\varepsilon$	Sudden	3.8
Prinos and Goulas (1993)	Re_D = 100,000 - 150,000	$k-\varepsilon$	Gradual	4.1
Yassen and Abdelhamed (2015)	-	RNG $k-\varepsilon$	Gradual	1.63, 2.54, 2.82, 3.14 and 5.19
Ahmed and Eljack (2014)	*Re* = 1,300,000 (based on test section height)	Spalart-Allmaras and $k-\omega$	Gradual	9
Mathew (2006)	Re_d = 4,400,000	$k-\omega$	Gradual	8, 10, 12 and 16
Wexler (2014)	Re_D = 10,000,000	Spalart-Allmaras, $k-\varepsilon$, $k-\omega$ and SST	Gradual	12.25
Sargison et al. (2004)	*Re* = 30,000 (based on test section width)	SST	Gradual	5.3
Abdelhamed et al. (2014)	Re_Θ = 2,169 and 2,774(based on momentum thickness at exit)	SST	Gradual	3.5 and 6.25
Bouriga et al. (2014)	Re_Θ = 5,000 (based on momentum thickness at exit)	SST	Gradual	9
Yu et al. (2012)	Re_d=50,000	$k-\varepsilon$, RNG $k-\varepsilon$, $k-\omega$, SST and RSM	Gradual	25

2.4 Previous works on optimization of contractions

As mentioned earlier, contractions are one of the critical components of wind tunnels as they are used to accelerate the flow. This in turn increases the velocity in the test section, improves flow uniformity and reduces the turbulence levels. Because of their importance, there have been numerous studies on optimization of contraction geometries. In the absence of separation within contractions, the flow can be adequately represented by Laplace equations for the stream function leading to analytical design of contractions with arbitrary shapes (Tsein, 1943; Szczenioeski, 1943; Smith and Wang, 1944; Thwaites, 1946). Some of these earlier methods of contraction design have been verified experimentally. For example, Tulapurkara (1980) experimentally studied Thwaite's method of contraction design and found satisfactory agreement with the literature.

As digital computers became widely available, alternative methods of contraction designs were possible by computing flow field as part of the contraction designs. For these studies, the most widely used design specifications for optimization of contractions were as follows: flow uniformity at contraction exit, avoidance of flow separation inside the contraction, minimum contraction length, and minimum exit boundary layer thickness. Morel (1975) carried out a study aimed at providing design guidelines and charts for axisymmetric contractions. He numerically simulated fluid flows inside contractions by specifying the contraction shapes. The contours of the contraction were obtained by two power law arcs joined smoothly together at specified inflection points. Finite difference solutions of the Euler equations were used to produce the design charts that defined contraction lengths and position of inflection points in terms of allowable adverse pressure gradient and desired flow uniformity. In another study, Morel (1977) carried out an inviscid fluid flow analysis of the maximum wall

pressure coefficients at inlet and exit of contractions by assuming a family of wall shapes made from two blended arcs. Mikhail (1979) proposed the optimum design of contractions defined to be the shortest length that avoids flow separation and has uniform exit flow. Bell and Mehta (1989) used three dimensional flow code adapted for internal fluid flows to optimize polynomial contraction curves and the results indicated that for a fifth order polynomial curve fit and a contraction ratio of 7.7, flow separation occurred for length to height ratios below 0.67 and above 1.79. They also observed that flow uniformity increased with increasing contraction length as the radius of curvature decreased. However, flow separation occurred for large contraction lengths by the effects of boundary layer thickening. Tulapurkara and Bhalla (1988) used Morel's contraction design method to design and test two contractions with contraction ratios 3.5 and 12. The measured values of boundary layer and flow uniformity were smaller than values predicted by Morel (1977). Fang (1997) extended Morrel's procedure to three dimensional square to square contraction case and developed a series of design charts. In addition, there are many other studies that have used Morel's design guidelines to optimize fluid flows through contractions (Fang et al., 2001; Mattos et al., 2003; Clark, 2010). Sargison et al. (2004) designed a two dimensional contraction using a sixth degree polynomial for a wind tunnel with a square working section. They observed that the flow quality improved by placing the inflection point as far downstream as possible. Ahmed and Eljack (2014) and Javed and Ali (2014) also used the sixth order polynomial to optimize their contraction shape. However, the location of inflection point was placed at the middle of the contraction by Ahmed and Eljack (2014) for their contraction design.

2.5 Summary

As discussed above, there are both practical and fundamental motivations to understand the characteristics of turbulent flows through contractions. In this chapter, the relevant experimental and numerical studies on fluid flows through contractions are reviewed. The effects of contraction on pressure losses, mean velocities and turbulence statistics have been studied extensively for sudden contractions and contractions with curved surfaces used for wind tunnel applications. The numerical studies showed the accuracy of RANS turbulence models to predict the mean velocity and turbulence characteristics for configuration of fluid flows through contractions. However, only a few studies have explored the flow characteristics through Tapered contractions such as a hopper. There has been a number of studies on optimization of contraction geometry for wind tunnel designs based on predefined design criteria. However, very few of them offer concrete and direct design information.

3 CHAPTER: EXPERIMENTAL SETUP AND MEASUREMENT PROCEDURE

In this chapter, an overview of the PIV system is presented. Also detailed description of the experimental setup, descriptions of the measurement procedure, test conditions, and measurement uncertainty are presented in this chapter.

3.1 Principles of PIV

The velocity measurements is obtained using a PIV system. The PIV is a non-intrusive velocity measurement technique that can provide instantaneous whole field velocity measurements. Because of its attractive features, PIV has been applied in numerous areas of fluid mechanics research. For this study a planar PIV is employed and therefore the principles of a planar PIV are outlined, and its various components are described.

A schematic setup for a planar PIV system is shown in Figure 3.1. The setup consists of a laser with generator (light source), charged couple device (CCD) camera (image recording device), test section with flow seeded with seeding particles, synchronizer for synchronisation of the camera and laser pulses, and computer system to store the digital images and post process the data. In the subsequent section the working principle of PIV is presented.

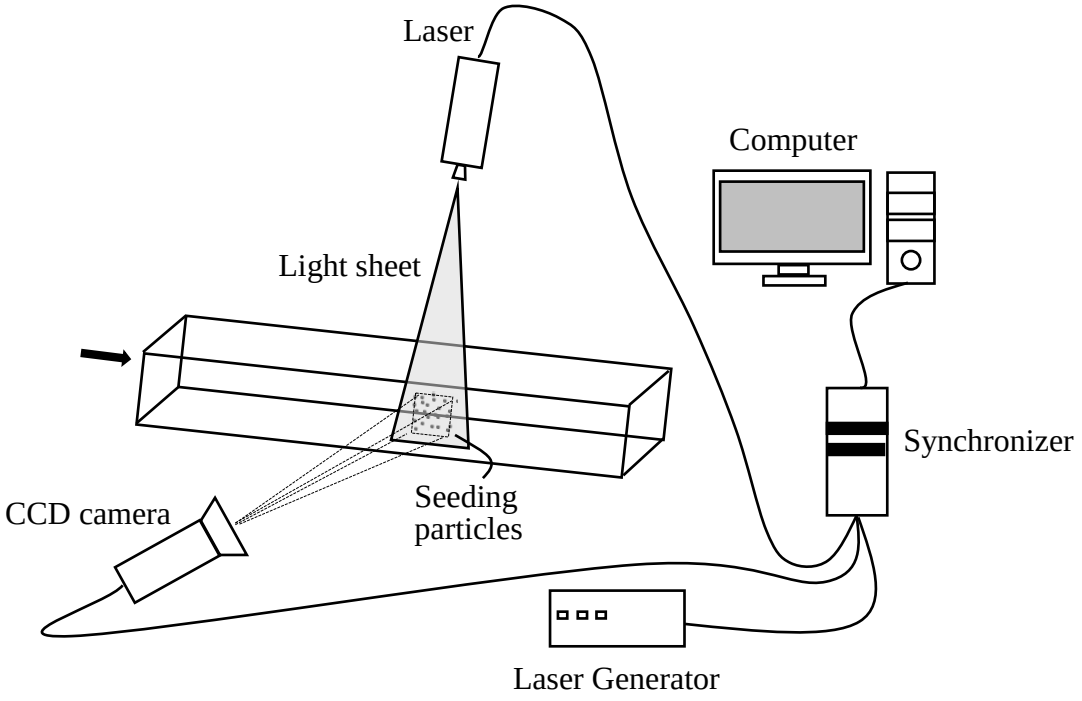

Figure 3.1: Schematic of a planar PIV system.

3.1.1 Planar PIV

The basic principle of PIV is based on seeding the flow with seeding particles that are assumed to follow the flow faithfully. A double pulsed laser is used to illuminate the seeding particles. The light emitted by the illuminated seeding particles is captured on a photographic film or with a CCD camera. The camera takes two snapshots of the flow within a short time interval which is known as the time between the laser pulses, Δt. The images captured are divided into grids of small areas known as interrogation area (IA). For each IA, a numerical correlation algorithm is applied to statistically determine the displacement vector (Δs) of the seeding particles from the two image pairs. The velocity field, v for each IA is determined from the expression $v = \Delta s/\Delta t$. The velocity field for the entire area is determined by repeating this for all the IA over the two image pairs. From the instantaneous velocity field, other flow quantities such as velocity gradients, vorticities and terms in the transport equations for the turbulent kinetic

energy and Reynolds stresses can be determined. The subsequent sections give descriptions of the characteristics of the seeding particles, the light source and the recording medium used in a typical planar PIV.

3.1.1.1 Seeding particles

Since PIV measures velocity of seeding particles not the fluid velocity it is essential to ensure that the particles follow the flow faithfully. Some of the important characteristics of seeding particles are as follows: the particles should be small enough to follow the flow faithfully but large enough to scatter sufficient light for them to be detected by the camera and the particles must be distributed homogenously. In addition, the seeding particles must have important hydrodynamic properties such as negligible settling velocity and settling time. The settling velocity can be estimated from Strokes drag law for flow around a sphere under gravity and is given by Mei et al. (1991),

$$v_s = \frac{(\rho_p - \rho_f) g d_p^2}{18 \mu_f} \tag{3.1}$$

where ρ_p is the particle density, ρ_f is the fluid density, g is the acceleration due to gravity, d_p is the diameter of the particle and μ_f is the viscosity of the fluid. The settling velocity can be reduced by using a seeding particle with smaller diameter and density similar to that of the working fluid.

The ability of particles to follow the flow is characterized by their response time. The response time of seeding particles gives a measure of the tendency of the particles to attain velocity equilibrium with the fluid. The response time for the particles is given by Raffel et al. (1998),

$$\tau_r = \rho_p \frac{d_p^2}{18\mu_f} \tag{3.2}$$

The seeding particles must also be good at scattering light to ensure that they are visible to the CCD sensor (Willert and Gharib, 1991). The particle size and shape, the refractive index and wavelength of radiation are factors that affect the light scattered by the particles. There are different seeding particles available for use depending on the type of flow that needs to be visualized. Some of the most widely used particles for liquids are polyamide seeding particles, silver coated hollow glass spheres, hollow glass spheres, polystyrene latex and fluorescent polymer particles.

3.1.1.2 Light source

The light source for the PIV must have very high intensity to illuminate the seeding particles so that the scattered light can be captured by the camera. For a planar PIV, the plane of light sheet is usually in the direction of the flow and the camera is mounted at a right angle to the laser plane. Frequency doubled neodymium-yttrium-aluminium-garnet (Nd:YAG) lasers are commonly used for PIV measurements because they provide monochromatic light with very high illumination. The light emitted by the laser is passed through the lens system to create a plane sheet of light to illuminate the region of interest. The length and width of the light sheet can be adjusted to the required field of view.

3.1.1.3 Recording medium

The CCD camera is the most widely used recording device for PIV. There are many advantages of CCD camera over photographic films. Some of the advantages of CCD camera are as follows: higher frame rates, possibility of on-line image analysis and higher resolution of pictures. The CCD camera has a major component called the CCD sensor which consists of an array of detectors called pixels. For PIV, the CCD chips

used in such cameras are high performance progressive scan interline type. These chips consist of an array of photographic cells that acquire the first image when the first laser pulse is triggered and then transfer this image to the storage cells. This allow the photographic cells to store the second image when the second laser pulse is triggered. Then the first and second images which are stored in the storage and photographic cells are sequentially transferred from the camera to the computer storage system. This allows the CCD camera exposure interval to be less than one microsecond.

3.2 Experimental setup

The experiments are conducted in the test facility shown in Figure 3.2. The facility is built and assembled at the University of Manitoba. The facility consists of a flow conditioning unit, Refuge One hopper supplied by RANA, circulating pump and piping, supporting framework, laser and CCD camera. The flow conditioning unit is 667 *mm* long, 309 *mm* wide and 300 *mm* deep. The unit contains series of sieves to break down large scale turbulence and straighten the flow prior to entering the hopper. Although the Refuge One uses air as the working fluid, water is used in the present facility for convenience.

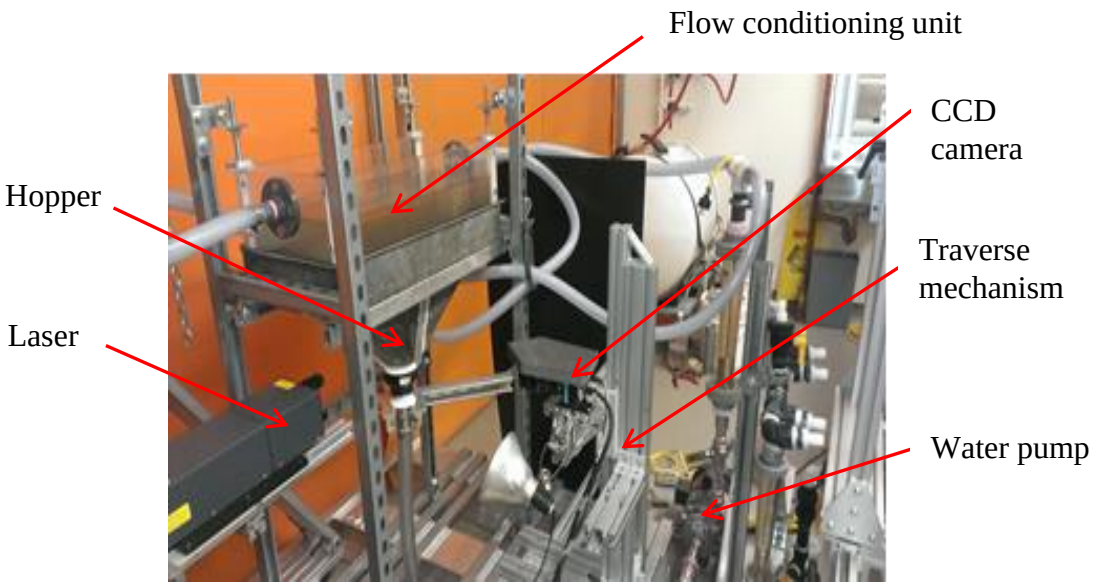

Figure 3.2: Experimental setup.

3.3 Test section

The test section is fabricated from a hopper of Refuge One. A picture of the Refuge One hopper is shown in Figure 3.3. The hopper is made from fiber glass. It has rectangular inlet which is 495 *mm* long, 195 *mm* wide, and height (*h*) of the hopper is 215 *mm*. The inlet section of the hopper transitions into a circular cross section at the exit plane with a diameter, d = 82 *mm*. The resulting contraction ratio is 18. A quarter of the hopper's symmetric section is cut and replaced with a transparent clear acrylic to facilitate velocity measurements using a PIV. The acrylic section is joined with the hopper by screwing it onto an aluminium metal plate. Polyurethane adhesive is used to seal any openings to ensure that the test section is water tight. During fabrication of the hopper, polyurethane adhesive used to seal the hopper exit connecting to a pipe prevented optical access at the exit. Figure 3.3 shows the modified hopper used to conduct the PIV measurements. A schematic of the test section with the transparent part represented by dotted lines is shown in Figure 3.4. The Cartesian coordinate system

adopted has the origin of the streamwise distance ($x = 0$) at the inlet and the origin of the wall-normal distance ($y = 0$) at the mid-section of the hopper.

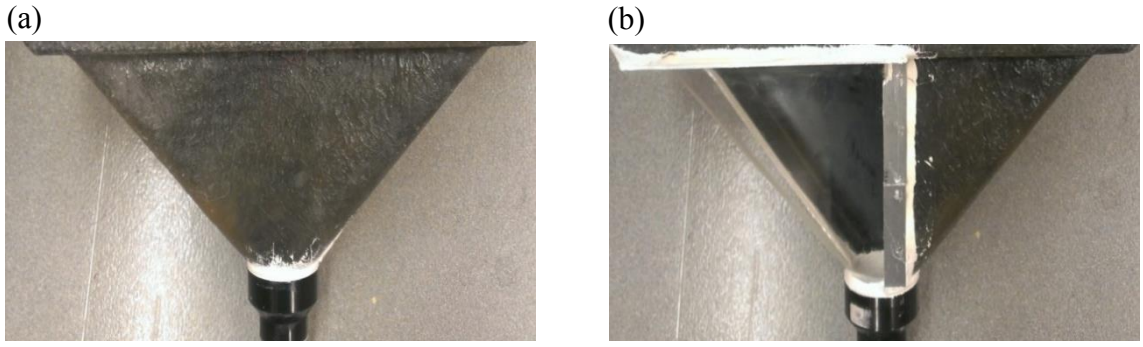

Figure 3.3: Hopper test section before (a) and after modification (b)

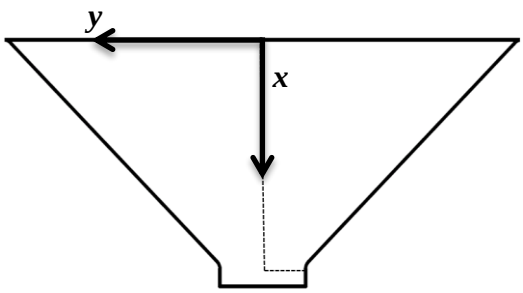

Figure 3.4: Schematic drawing of hopper test section.

3.3.1 Measurement procedure

A PIV is used to conduct velocity measurements in the *x-y* plane located at the mid-span of the test section. In the present study, the working fluid (i.e. water) is seeded with 10 μm silver coated hollow glass spheres having specific gravity of 1.4. The settling velocity of the particles is estimated from Equation (3.1) to be 0.22 $\mu m/s$, which is significantly smaller than the velocity of the flow. Also, the response time of the seeding particles is estimated from Equation (3.2) to be 7.76 μs. The settling velocity and the response time show that the seeding particles follow the flow faithfully.

An Nd-YAG double pulsed laser with pulse energy of 120 *mJ/pulse* that emits a green light at a wavelength of 532 *nm* is used to illuminate the flow field. Because a quarter part of the test section is made with acrylic material the laser is shot from the side of the test section through the transparent part. The light sheet is aligned with the mid-section of the hopper. The scattered light from the seeding particles is captured by a 12-*bit* HiSense 4M CCD camera with 2048 *pixels* × 2048 *pixels* CCD array size and 7.4*μm* pixel pitch. The camera is fitted with 60 *mm* AF Micro Nikkor lens. The images captured are stored on a hard disk. The field of view of the camera is set to 108 *mm* × 108 *mm* in the *x*-*y* plane. Four different measurement planes (P1-P4) are used to map out the transparent quarter of the flow domain as shown in Figure 3.5.

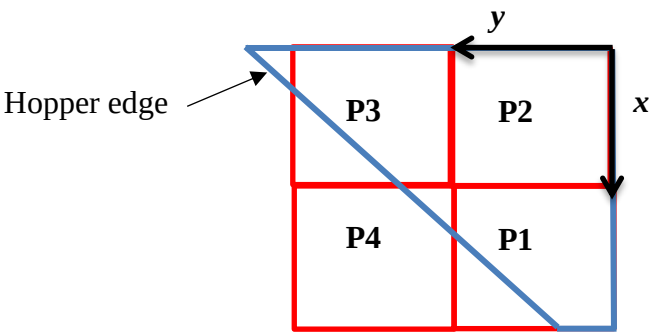

Figure 3.5: Measurement planes (P1-P4).

Based on a preliminary convergence test, a sample size of 6000 instantaneous image pairs are acquired in each plane. The 6000 image pairs used in the present study are substantially greater than 1047 image pairs used by Sanchez et al. (2010), for example, to compute the mean velocities in sudden contraction flows. The instantaneous images are post processed using the adaptive correlation and moving average validation options of the commercial software Dynamic Studio version 3.41 developed by Dantec Dynamics Inc. The IA size for the adaptive correlation is set to 64 *pixels* × 64 *pixels* with 50 % overlap in both the *x* and *y* directions. The adaptive correlation uses a multi-

pass fast Fourier transform cross-correlation algorithm to determine the average particle displacement within the interrogation area. A three point Gaussian curve fit is used to determine particle displacement with subpixel accuracy. The moving average validates or rejects vectors based on a comparison between neighbouring vectors. The rejected vectors are then replaced by vectors estimated from surrounding values. The particle image diameter is estimated to be d_p = 1.61 *pixels*, a value that is close to the recommended optimum value of d_p = 2 *pixels* recommended by Raffel et al. (1998) to avoid peak locking.

3.4 Test conditions

As mentioned earlier, water is used as the working fluid instead of air for convenience. However, the concept of Reynolds number similarity is employed to minimize any effect of Reynolds number on the mean and turbulence statistics that may arise from differences in working fluid used. Upon consultation with RANA engineers, it is found that the operating flow rate of the blower used in the Refuge One is 0.0519 m^3/s which results in Reynolds number based on the maximum exit velocity of air (U_{max} = 9.83 *m/s*) and exit diameter of the hopper (d = 0.082 *m*), Re_d = 53,000. Following Reynolds number similarity, the equivalent flow rate and maximum exit velocity when water is used as working fluid are Q = 0.0034 m^3/s and U_{max} = 0.65 *m/s*, respectively. Therefore, the experiment is performed at Q = 0.0034 m^3/s and Re_d = 53,000. Another experiment is conducted at a flow rate of 0.0015 m^3/s and Re_d = 23,000 to investigate any possible effects of Reynolds number on the flow characteristics. For simplicity, the experiments conducted at Re_d = 53,000 and 23,000 are hereafter referred to as $Re_{d\text{-}53}$ and $Re_{d\text{-}23}$ respectively. The corresponding maximum exit velocities for test conditions $Re_{d\text{-}53}$ and $Re_{d\text{-}23}$ are U_{max} = 0.65 *m/s* and 0.28 *m/s*, respectively.

3.5 Measurement uncertainty

The measurement uncertainty is performed following the guidelines of AIAA standard described by Coleman and Steele (1995). The total error is defined as the sum of bias and precision errors. Bias error is the systematic error and the precision error contributes to the scatter of the data. Detailed procedure for calculating the bias and precision errors for PIV measurements is described by Prasad et al. (1992) and Forliti et al. (2000). Therefore, this will not be repeated here. On the basis of the size of the interrogation area and Gaussian fit curve used to calculate the instantaneous vector maps, which are then used to calculate the mean velocities at 95% confidence level, the uncertainties are estimated to be $\pm$2%, $\pm$4% for U and V, respectively, in the near wall region. The uncertainties in the turbulence intensities and Reynolds stress are, respectively, estimated to be $\pm$7%, $\pm$10% of the peak values.

4 CHAPTER: NUMERICAL PROCEDURE AND MODELLING

This chapter presents a description of the governing equations, the various turbulence models ($k-\varepsilon$ model, RNG $k-\varepsilon$ model, $k-\omega$ model, $k-\omega$ based SST model and Reynolds stress model (RSM)) and numerical procedure used to perform numerical modelling of flow through the Refuge One hopper using a commercial CFD code ANSYS CFX 15.0.

4.1 Governing equations

The RANS equations for continuity and momentum conservation for a three-dimensional steady state incompressible turbulent flow can be written as:

$$\frac{\partial U_j}{\partial x_j} = 0 \tag{4.1}$$

$$\frac{\partial}{\partial x_j}\left(\rho U_j U_i\right) = -\frac{\partial P}{\partial x_i} + \frac{\partial}{\partial x_j}\left(\mu \frac{\partial U_i}{\partial x_j} - \rho u_i u_j\right) \tag{4.2}$$

where U_j and u_i denote the mean and fluctuating velocity components in the x_i direction, ρ is the density, μ is the dynamic viscosity, P is the pressure and $u_i u_j$ is the Reynolds stress tensor.

As a result of averaging, the Reynolds stress tensor $u_i u_j$ appears in the above set of governing equations. The tensor is symmetric and it represents correlation between fluctuating velocities. It is an additional term due to turbulence and it is unknown, therefore, the appearance of Reynolds stress tensor introduces a closure problem. That is, the number of unknowns (a total of ten unknowns comprising three velocity components, pressure and six independent stresses from the Reynolds stress tensor) is larger than the number of equations (continuity and momentum). There is a need for

additional equations that relate the Reynolds stress tensor to known quantities; however, no such equations exits. Closure of Equation (4.2), therefore, requires modelling of the unknown Reynolds stress tensor. Various turbulence models have been developed to represent the Reynolds stresses in terms of the mean flow quantities and some turbulence parameters.

4.2 Turbulence modelling

In this study, five turbulence models are used. These include four two-equation turbulence models, and one Reynolds stress model. The two-equation models are the $k-\varepsilon$ model developed by Launder and Spalding (1974), RNG $k-\varepsilon$ model by Yakhot et al. (1992), $k-\omega$ model by Wilcox (1986) and $k-\omega$ based SST model by Menter (1994). The Reynolds stress model is the ε based second moment closure model developed by Launder et al. (1975). In the following sections, a brief overview of the turbulence models is presented.

4.2.1 Eddy viscosity based models

For the two-equation turbulence models used in this study, the Reynolds stresses are linearly related to the mean rate of strain by eddy viscosity as follows:

$$-\rho u_i u_j = \mu_t \left(\frac{\partial U_i}{\partial x_j} + \frac{\partial U_j}{\partial x_i}\right) - \frac{2}{3}\rho\delta_{ij}k \tag{4.3}$$

where μ_t is the eddy viscosity, δ_{ij} is the Kronecker delta and k is the turbulent kinetic energy. In the solution of the model equations, the pressure is the thermodynamic pressure plus $\frac{2}{3}\rho\delta_{ij}k$. The $k-\varepsilon$ model, RNG $k-\varepsilon$ model, $k-\omega$ model and $k-\omega$ based SST turbulence models are briefly summarized below.

4.2.1.1 The $k-\varepsilon$ model

The $k-\varepsilon$ model consists of the following two transport equations for the turbulent kinetic energy, k, and its dissipation rate, ε, given by:

$$\frac{\partial}{\partial x_j}(\rho U_j k) = \frac{\partial}{\partial x_j}\left(\left(\mu + \frac{\mu_t}{\sigma_k}\right)\frac{\partial k}{\partial x_j}\right) + P_k - \rho\varepsilon \tag{4.4}$$

$$\frac{\partial}{\partial x_j}(\rho U_j \varepsilon) = \frac{\partial}{\partial x_j}\left(\left(\mu + \frac{\mu_t}{\sigma_\epsilon}\right)\frac{\partial \varepsilon}{\partial x_j}\right) + \frac{\varepsilon}{k}(C_{\varepsilon 1}P_k - C_{\varepsilon 2}\rho\varepsilon) \tag{4.5}$$

where the production term, P_k is:

$$P_k = \mu_t\left(\frac{\partial U_i}{\partial x_j} + \frac{\partial U_j}{\partial x_i}\right)\frac{\partial U_i}{\partial x_j} \tag{4.6}$$

and the eddy viscosity is computed using $\mu_t = C_\mu \rho k^2/\varepsilon$. The $k-\varepsilon$ model constants are as follows: $C_{\varepsilon 1}$ = 1.44, $C_{\varepsilon 2}$ = 1.92, σ_k = 1.0, σ_ϵ = 1.3 and C_μ = 0.09.

4.2.1.2 The RNG $k-\varepsilon$ model

The RNG $k-\varepsilon$ model is developed using re-normalisation group (RNG) methods to renormalize the Navier-Stokes equations to account for the effect of smaller scales of turbulence. Compared to the $k-\varepsilon$ model, the RNG $k-\varepsilon$ model calculates the model constants explicitly and contains additional terms in the transport equations. The RNG approach has a similar transport equation for turbulent kinetic energy but has a modified transport equation for the dissipation rate, which attempts to take into account the different scales of turbulence through changes to the production term. The modified form of the ε equation is given by:

$$\frac{\partial}{\partial x_j}(\rho U_j \varepsilon) = \frac{\partial}{\partial x_j}\left(\left(\mu + \frac{\mu_t}{\sigma_{\varepsilon RNG}}\right)\frac{\partial \varepsilon}{\partial x_j}\right) + \frac{\varepsilon}{k}(C_{\varepsilon 1RNG} P_k - C_{\varepsilon 2RNG}\rho\varepsilon) \quad (4.7)$$

with

$$C_{\varepsilon 1RNG} = 1.42 - f_\eta \quad (4.8)$$

$$f_\eta = \frac{\eta\left(1 - {}^{\eta}/_{4.38}\right)}{(1 + \beta_{RNG}\eta^3)} \quad (4.9)$$

$$\eta = \sqrt{\frac{P_k}{\rho C_{\mu RNG}\varepsilon}} \quad (4.10)$$

where the eddy viscosity is calculated in the same manner as with the $k - \varepsilon$ model. The RNG $k - \varepsilon$ model constants are as follows: $C_{\varepsilon 2RNG}$ = 1.68, $C_{\mu RNG}$ = 0.085, $\sigma_{\varepsilon RNG}$= 0.7179 and β_{RNG}= 0.012.

4.2.1.3 The $k - \omega$ model

The $k - \omega$ model has a near wall treatment capability in CFX that allows the model to use finer meshes near the wall. It consists of the following two transport equations for turbulent kinetic energy, k, and specific turbulence dissipation, ω:

$$\frac{\partial}{\partial x_j}(\rho U_j k) = \frac{\partial}{\partial x_j}\left(\left(\mu + \frac{\mu_t}{\sigma_k}\right)\frac{\partial k}{\partial x_j}\right) + P_k - \rho\beta^* k\omega \quad (4.11)$$

$$\frac{\partial}{\partial x_j}(\rho U_j \omega) = \frac{\partial}{\partial x_j}\left(\left(\mu + \frac{\mu_t}{\sigma_\omega}\right)\frac{\partial \omega}{\partial x_j}\right) + \alpha\frac{\omega}{k}P_k - \rho\beta\omega^2 \quad (4.12)$$

where P_k is the same as in the $k-\varepsilon$ model. The eddy viscosity is computed using $\mu_t = \rho k/\omega$ and the $k-\omega$ model constants are as follows: β^* = 0.09, α = 5/9, β = 0.075, σ_k and σ_ω = 2.

4.2.1.4 The $k-\omega$ based SST model

The $k-\omega$ based SST model combines the $k-\varepsilon$ and $k-\omega$ models using a blending function. This allows the SST model to activate $k-\omega$ model in the near wall region and $k-\varepsilon$ model for the rest of the flow. By doing this, the higher performance of $k-\omega$ model is utilized. The equations for the $k-\omega$ based SST model are:

$$\frac{\partial}{\partial x_j}(\rho U_j k) = \frac{\partial}{\partial x_j}\left(\left(\mu + \frac{\mu_t}{\sigma_{k2}}\right)\frac{\partial k}{\partial x_j}\right) + P_k - \rho\beta^* k\omega \tag{4.13}$$

$$\frac{\partial}{\partial x_j}(\rho U_j \omega) = \frac{\partial}{\partial x_j}\left(\left(\mu + \frac{\mu_t}{\sigma_{\omega 3}}\right)\frac{\partial \omega}{\partial x_j}\right) + (1-F_1)2\rho\frac{1}{\sigma_{\omega 2}\omega}\frac{\partial k}{\partial x_j}\frac{\partial \omega}{\partial x_j} + \alpha_3\frac{\omega}{k}P_k - \rho\beta_3\omega^2 \tag{4.14}$$

where $\beta^*, \alpha_1, \beta_1, \sigma_{k1}, \sigma_{\omega 2}, \alpha_2, \beta_2, \sigma_{k2}$ and $\sigma_{\omega 2}$are model constants with values 0.09, 5/9, 0.075, 2, 2, 0.44, 0.0828, 1 and 1/0.856, respectively. All other symbols have their usual meaning and blending function, F_1 is:

$$F_1 = \tanh(\arg_1^4) \tag{4.15}$$

with

$$\arg_1 = \min\left(\max\left(\frac{\sqrt{k}}{\beta^*\omega y}, \frac{500\nu}{y^2\omega}\right), \frac{4\rho k}{CD_{k\omega}\sigma_{\omega 2}y^2}\right) \tag{4.16}$$

$$CD_{k\omega} = \max\left(2\rho\frac{1}{\sigma_{\omega 2}\omega}\frac{\partial k}{\partial x_j}\frac{\partial \omega}{\partial x_j}, 1.0\times 10^{-10}\right) \tag{4.17}$$

The distance of the first nodal point away from the wall is y, and ν is the kinematic viscosity. The formulation of the eddy viscosity is given by:

$$\mu_t = \frac{\rho\alpha_1 k}{\max(\alpha_1\omega, SF_2)} \tag{4.18}$$

with $F_2 = \tanh(arg_2^2)$ and $arg_2 = \max\left(\frac{2\sqrt{k}}{\beta^*\omega y}, \frac{500\nu}{y^2\omega}\right)$, where F_2 is a blending function similar to F_1 and S is an invariant measure of the strain rate, given by:

$$\mathrm{S} = \sqrt{\left(\frac{\partial U_j}{\partial x_i} + \frac{\partial U_i}{\partial x_j}\right)\frac{\partial U_i}{\partial x_j}} \tag{4.19}$$

4.2.2 Reynolds stress model (RSM)

In contrast to the two-equation turbulence models where the Reynolds stresses are based on the eddy viscosity hypothesis, the RSM model calculates the Reynolds stresses directly from their respective transport equations. In RSM, six transport equations are solved to obtain the six Reynolds stresses along with the transport equation for calculating the turbulence dissipation rate. The RSM adopted in the present study is based on the ε equation. The Reynolds stress transport equations are expressed as:

$$\frac{\partial}{\partial x_k}\left(U_k\rho u_i u_j\right) = \frac{\partial}{\partial x_k}\left(\left(\mu + \frac{2}{3}C_s\rho\frac{k^2}{\varepsilon}\right)\frac{\partial u_i u_j}{\partial x_k}\right) - \partial\rho u_k u_i\frac{\partial U_j}{\partial x_k} - \partial\rho u_k u_j\frac{\partial U_i}{\partial x_k} + \phi_{ij} - \frac{2}{3}\delta_{ij}\rho\varepsilon \tag{4.20}$$

The pressure-strain term, ϕ_{ij}, is modelled using:

$$\phi_{ij} = -\rho\varepsilon C_{s1} a_{ij} + C_{r2}\rho k s_{ij} + C_{r4}\rho k\left(a_{ik}S_{jk} + a_{jk}S_{ik} - \frac{2}{3}\delta_{ij}S_{kl}a_{kl}\right) + C_{r5}\rho k(a_{ik}W_{jk} + a_{jk}W_{ik}) \quad (4.21)$$

where

$$a_{ij} = \frac{u_i u_j}{k} - \frac{2}{3}\delta_{ij} \quad (4.22)$$

$$S_{ij} = \frac{1}{2}\left(\frac{\partial U_i}{\partial x_j} + \frac{\partial U_j}{\partial x_i}\right) \quad (4.23)$$

$$W_{ij} = \frac{1}{2}\left(\frac{\partial U_i}{\partial x_j} - \frac{\partial U_j}{\partial x_i}\right) \quad (4.24)$$

are the anisotropy, mean rate of strain and mean vorticity tensors, respectively. The dissipation rate equation that is solved with Reynolds stress model is:

$$\frac{\partial}{\partial x_k}(\rho U_k \varepsilon) = \frac{\partial}{\partial x_k}\left(\left(\mu + \frac{\mu_t}{\sigma_\varepsilon}\right)\frac{\partial \varepsilon}{\partial x_k}\right) + \frac{\varepsilon}{k}\left(C_{\varepsilon 1}\left(-\rho u_i u_j \frac{\partial U_i}{\partial x_k}\right) - C_{\varepsilon 2}\rho\varepsilon\right) \quad (4.25)$$

The Reynolds stress model constants are as follows: C_s = 0.22, C_{s1} = 1.8, C_{r2} = 0.8 , C_{r4} = 0.6, C_{r5} = 0.6, $C_{\varepsilon 1}$ = 1.45, $C_{\varepsilon 2}$ = 1.9 and σ_ε = 1.10.

4.3 CAD geometry

A 3D laser scan of the interior surface of the hopper using Creamfirm EXAscan is performed at the Industrial Technology Center near the University of Manitoba. As mentioned in Chapter 3, Refuge One hopper is fitted with an acrylic section that is joined to the fiberglass hopper body with an aluminium plate. Also an extended pipe is attached at the exit of the hopper. It is ensured that after this modification the inner surface of the hopper is smooth; however there are slight discontinuities along the

joined surfaces. During the 3D scanning process, all the discontinuities are smoothened to simplify data post processing. The scanned data are then imported into Autodesk Inventor 2014 in an STL file format and a CAD model of the hopper geometry is generated from this data.

4.4 Mesh configuration

In this study, ANSYS CFX-Mesh is used to generate the mesh for the numerical simulation. Unstructured, non–orthogonal, non–uniform grids are generated for discretizing the computational domain. The grids are created using body sizing and inflation option to account for the boundary layer growth along the walls of the hopper and pipe. The grid independence is checked using four different grid densities to ensure that grid resolution does not have a notable impact on the numerical results.

Specific to the hopper, the mesh used in the regions with larger velocity gradients should be sufficiently fine to capture the local small scale flow physics. On the other hand, to reduce the computational expenses, relatively coarse meshes should be applied to the rest of the domain. In the near wall region of the hopper there are relatively large velocity gradients because of boundary layer development. For this reason, the height of the first node is kept at $1.0\times10^{-5}\,m$ with an expansion factor of 1.15. This ensures that the dimensionless distance from the wall (y^+) is less than one, which is recommended for boundary layer flows in CFX. Also, to reduce computational expense, sphere of influence of varying sizes are tested before selecting a sphere with radius $0.3\,m$. Smaller element size is used within the sphere which contains the hopper and for the remaining part of the computational domain outside the sphere which includes the attached pipe, relatively large element size is used. Thus, significant reduction in mesh requirements is achieved without compromising on the quality of mesh for the most important part

of the computational domain (i.e., hopper) for this study. The mesh configuration of the computational domain is shown in Figure 4.1.

(a)

(b)

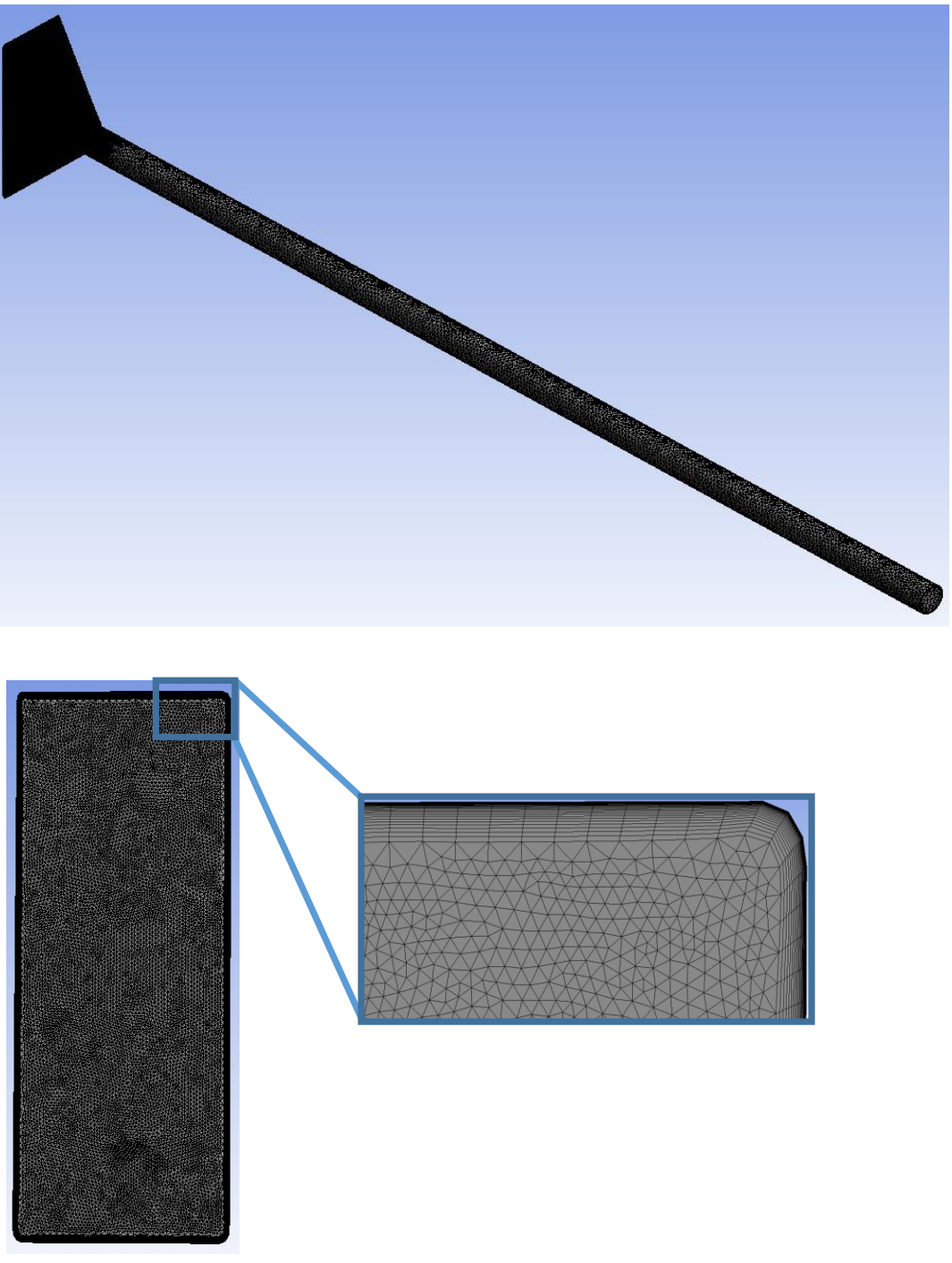

Figure 4.1: Mesh configuration of the computational domain (a) Plan view of the hopper inlet with inset showing the zoomed mesh configuration (b).

4.5 Numerical method

The numerical solution of the governing equations is obtained using a commercial CFD code, ANSYS CFX 15.0. In this code, the governing equations are solved by subdividing the fluid domain into finite number of cells and the equations are changed into algebraic form via discretization process based on a finite volume method (FVM). Versteeg and Malalasekera (2007) provided an extensive review of the FVM used in the CFX code. A collocated grid is used where the values of all the variables are calculated at cell centers. To prevent decoupling of the velocity and pressure fields, mass conservation discretization is applied using the Rhie and Chow (1983) interpolation algorithm. The semi-implicit method for pressure-linked equations algorithm is used to couple the pressure and velocity. High resolution advection scheme based on the work of Barth and Jespersen (1989) is used for discretizing the advection terms. The discretized mass, momentum and turbulence model equations is solved iteratively using an additive correction multi-grid method to accelerate convergence. For this study, double precision is used in all the computations and the solution is considered converged when the normalized residual of each of the discretized equations is less than 1.0×10^{-6}.

4.6 Boundary conditions

Appropriate prescription of boundary conditions is critically important to obtain correct and reliable results from a numerical simulation. Different types of boundary conditions that are used are explained in this section.

The boundary conditions for the solution domain are shown in Figure 4.2. At the inlet, a constant mass flow rate, $\dot{m}$ = 3.15 *kg/s* is specified corresponding to test condition $Re_{d\text{-}53}$. In addition, at the inlet the relative turbulence intensity is set to 5% based on the

experimental results. At the outlet, the average static pressure is set to zero and the outlet is specified at a distance of 4 m (48 d) downstream from the hopper exit. This distance is chosen to ensure that a fully developed turbulent flow condition is achieved at the outlet. A no-slip boundary condition is prescribed along hopper and pipe walls. In $k-\varepsilon$ model, RNG $k-\varepsilon$ model and RSM a scalable wall-function is used. A near wall treatment with automatic switch from wall-function to a low Reynolds number formulation based on grid refinement is employed for the $k-\omega$ model and $k-\omega$ based SST model. It should be noted that for all the turbulence models $y^{+}<1$ is maintained. The Cartesian coordinate system adopted for the numerical simulation is the same as described in Chapter 3.

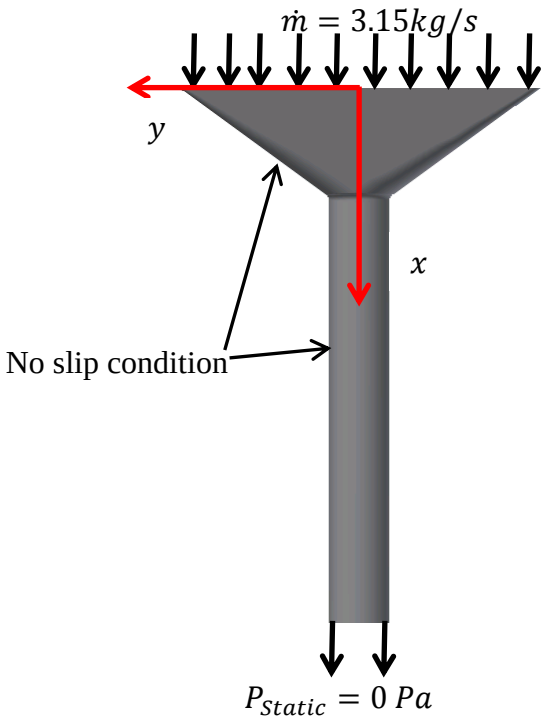

Figure 4.2: Boundary conditions used for the computational domain.

4.7 Grid independent tests

The grid dependence is checked using four different grid densities to ensure that grid resolution does not have notable impact on the numerical results. The grid

independence tests are conducted using four different grids which are as follows: grid A with 1,866,246 elements, grid B with 3,837,910 elements, grid C with 5,299,553 elements and grid D with 6,011,243 elements. As mentioned earlier in section 4.4, the solutions are considered converged when the sum of the normalized residuals for each of the discretized equations is less than 1.0×10^{-6}.

Based on the area averaged streamwise velocity at the hopper exit, streamwise and wall-normal mean velocity profiles extracted at midpoint and exit of the hopper (x/h = 0.5 and 1) and area averaged pressure difference between inlet and exit of the hopper, the maximum differences between the four different grids for $k-\omega$ based SST model are presented in Table 4.1. Based on these results, grid C is selected for the present investigation using $k-\omega$ based SST model. The grid independence tests using the four computational grids discussed above are extended to the remaining two-equation models and RSM. These grid independent results will not be shown here because the results are similar to $k-\omega$ based SST model. Based on the results, grid C is also selected for the present investigation using $k-\varepsilon$ model, RNG $k-\varepsilon$ model, $k-\omega$ model and RSM.

Table 4.1: Grid independence test results for maximum percentage differences between four grids (grids A-D) for area averaged streamwise mean velocity at hopper exit, streamwise and wall-normal mean velocity profiles at two locations (x/h = 0.5 and 1) and area averaged pressure difference between the inlet and exit of the hopper for $k-\omega$ based SST model.

Grids	Streamwise velocity at hopper exit	Streamwise velocity at *x/H*		Wall-normal velocity at *x/H*		Pressure difference
		0.5	1	0.5	1	
A and B	-0.20%	-1.16%	-3.00%	-1.09%	-4.92%	1.43%
B and C	0.02%	-0.72%	0.60%	-0.93%	3.87%	0.51%
C and D	-0.01%	-0.03%	0.05%	0.07%	-0.74%	0.08%

5 CHAPTER: RESULTS AND DISCUSSIONS

In the first part of this chapter, the experimental results are presented and discussed. In this section, contour plots of mean velocities and turbulent statistics are presented to visualize the flow characteristics through the Refuge One hopper. This is followed by Section 5.2 which presents the numerical results. In this section, contour plots of mean velocities and profiles of mean velocities at selected streamwise locations are compared against the experimental results to assess the predictions of different turbulence models. In Section 5.3, comparison of mean velocities, pressure coefficient, skin friction coefficient and head losses for different hopper geometries are presented to quantify the effect of hopper height and wall shape on flow characteristics and energy loss.

5.1 Experimental results

5.1.1 Contour plots of mean velocities

In this section, contour plots of the streamwise and wall-normal mean velocities for two Reynolds numbers (Re_d = 53,000 and 23,000) are presented and discussed. For brevity, the two Reynolds number will be referred to as $Re_{d\text{-}53}$ and $Re_{d\text{-}23}$ hereafter. The contour plots are used to visualize the flow characteristics through the Refuge One hopper as well as examine the effect of Reynolds number on the flow statistics. In each of the contour plots, the streamwise and wall-normal distances are normalized by the exit diameter of the hopper, d. The streamwise and wall-normal mean velocities are normalized by the maximum streamwise exit velocity, U_{max}.

Figure 5.1 shows the contour plots of the streamwise mean velocities obtained from the PIV measurements for $Re_{d\text{-}53}$ and $Re_{d\text{-}23}$. The contour plots of the mean velocities obtained in the four planes of measurement are combined to obtain a whole field visualization of the flow field. For each test condition, the streamwise mean velocity

accelerates with increasing streamwise distance until the maximum velocity occurs near the exit of the hopper. The acceleration of the flow with the increasing streamwise distance is caused by the gradual contraction of the hopper. The flow pattern near the exit of the test section is qualitatively similar for the two flow conditions investigated. Similar results were also obtained by Prinos and Goulas (1993) for a gradual contraction with upstream Reynolds numbers 100,000 and 150,000, respectively.

The contour plots of the wall-normal mean velocities for $Re_{d\text{-}53}$ and $Re_{d\text{-}23}$ are shown in Figure 5.2. As can be seen, the maximum wall-normal mean velocity occurs close to the wall and near the exit of the hopper. At the centerline of the hopper, the wall-normal mean velocity is identically zero. For the higher Reynolds number flow ($Re_{d\text{-}53}$) the maximum wall-normal mean velocity is 10% higher. The gradual transition from a wider cross-sectional area at the inlet of the hopper to a smaller circular cross-section at the exit plane causes a gradual increase in the mean velocities with the increasing streamwise distance.

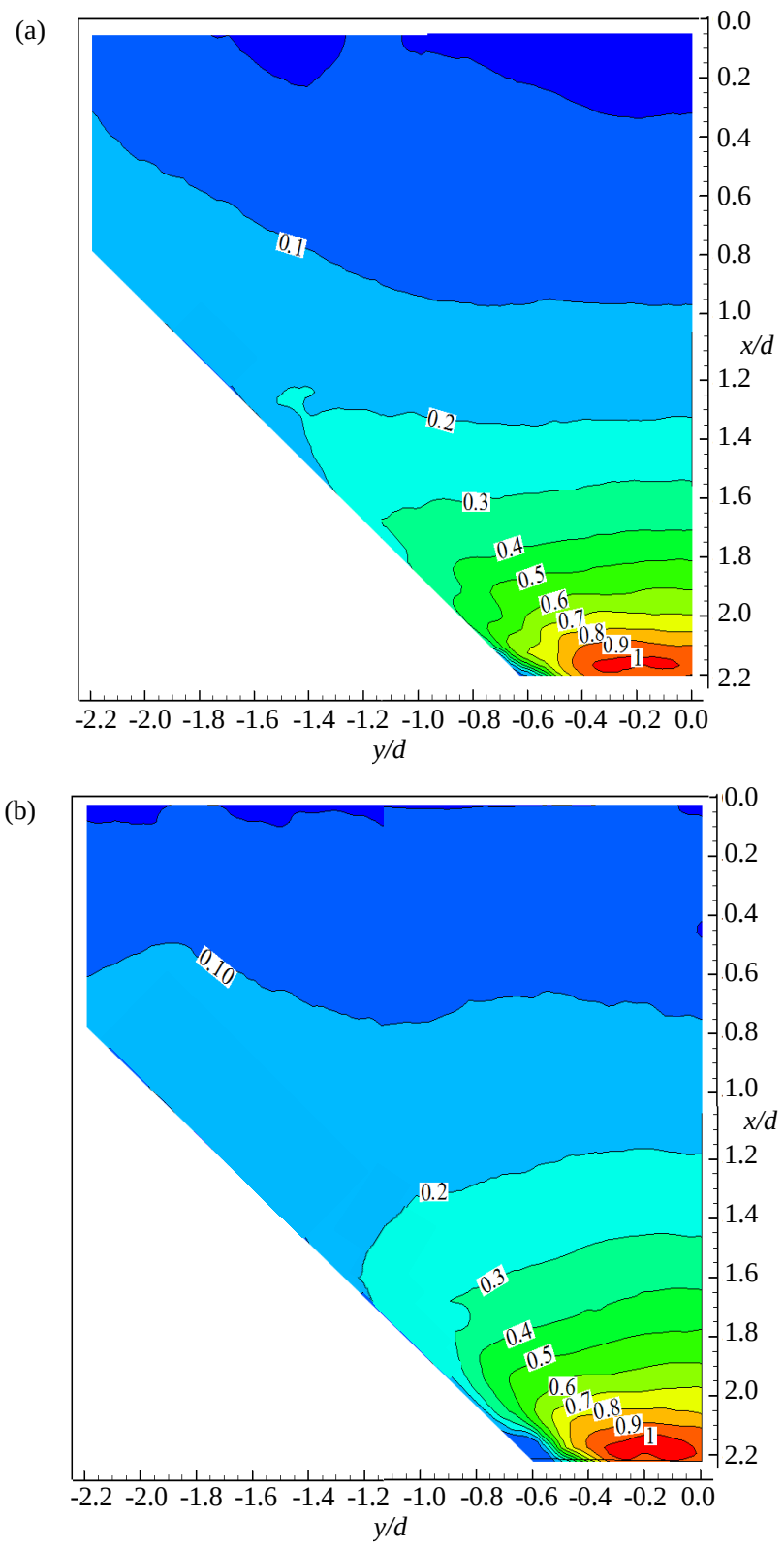

Figure 5.1: Contour plots of streamwise mean velocities for $Re_{d\text{-}53}$ (a) and $Re_{d\text{-}23}$ (b).

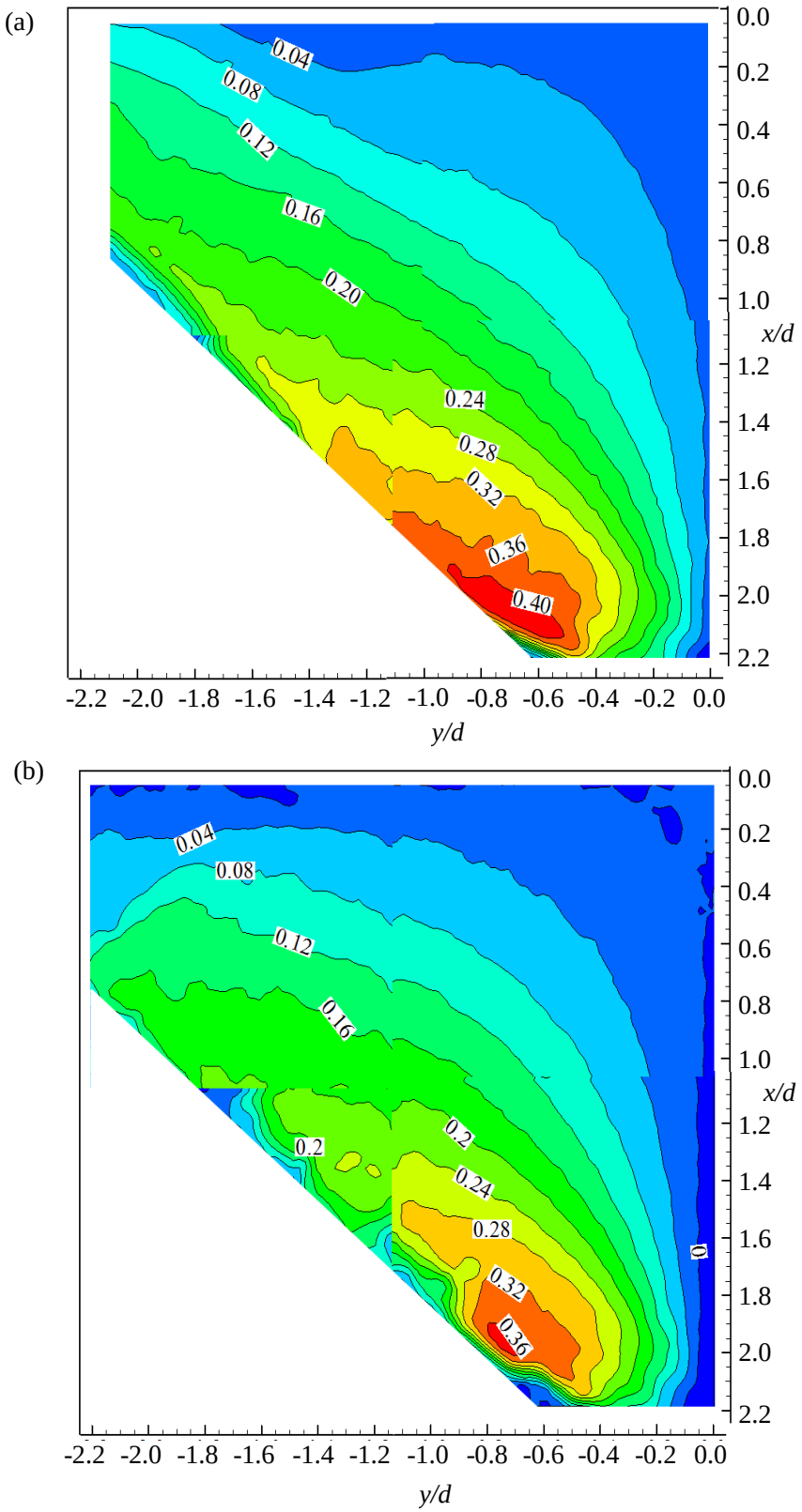

Figure 5.2: Contour plots of wall-normal mean velocities for $Re_{d\text{-}53}$ (a) and $Re_{d\text{-}23}$ (b).

5.1.2 Contour plots of turbulent quantities

Contour plots of turbulent kinetic energy (k) and Reynolds shear stress ($-uv$) for $Re_{d\text{-}53}$ and $Re_{d\text{-}23}$ are presented in Figures 5.3 and 5.4 to examine the turbulence field through the Refuge One hopper. Since, the spanwise Reynolds stress, w^2 is not measured in the present study, the turbulent kinetic energy is approximated as $k = 0.75(u^2+v^2)$. The contour plots are shown only for plane 1 as the maximum values are observed in this plane. The contours of turbulent kinetic energy are qualitatively similar for both flow conditions. The maximum turbulent kinetic energy occurs near the exit of the hopper. The contours of Reynolds shear stress are also qualitatively similar for $Re_{d\text{-}53}$ and $Re_{d\text{-}23}$. The location of the minimum value of Reynolds shear stress is located near the wall at the exit of the hopper.

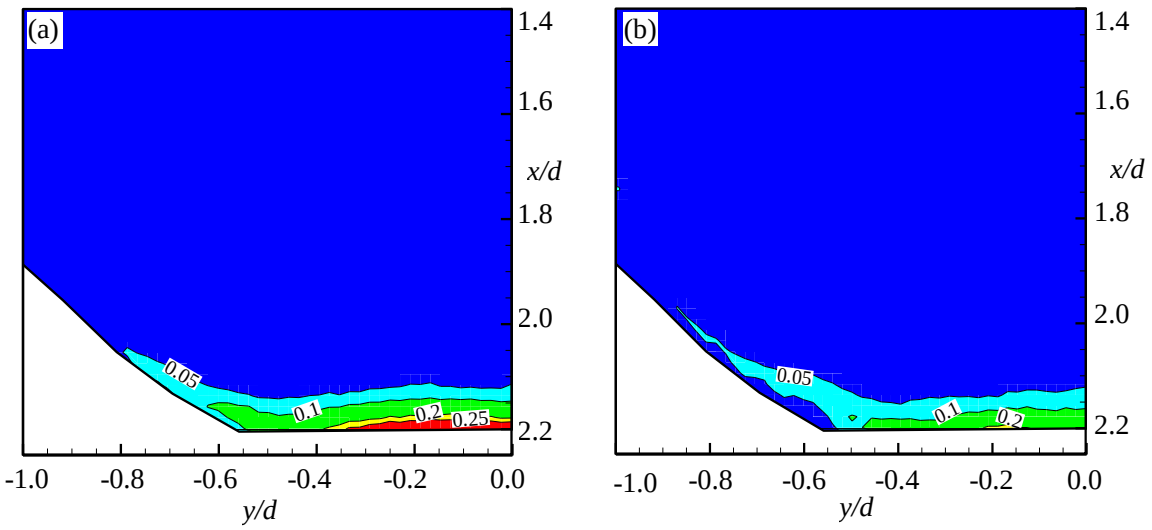

Figure 5.3: Contour plots of turbulent kinetic energy, k for $Re_{d\text{-}53}$ (a) and $Re_{d\text{-}23}$ (b).

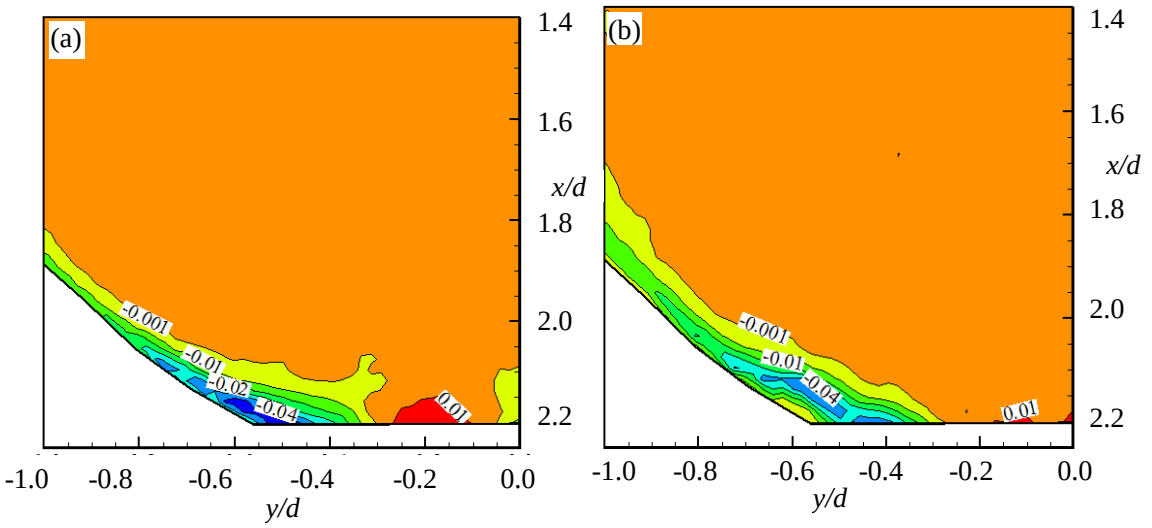

Figure 5.4: Contour plots of Reynolds shear stress, $-uv$ for $Re_{d\text{-}53}$ (a) and $Re_{d\text{-}23}$ (b).

5.2 Numerical results

In this section, $k-\varepsilon$, RNG $k-\varepsilon$, $k-\omega$, $k-\omega$ based SST and RSM turbulence models discussed in Chapter 4 are used to predict the experimental data. The quantities predicted are the streamwise and wall-normal mean velocities at selected *x/d* locations. This will help in assessing the performance of the turbulence models in predicting these quantities.

5.2.1 Contour plots of mean velocities

For comparison with the experimental data, contours of the streamwise and wall-normal mean velocities are presented in this section. The contours predicted by the five different turbulence models are qualitatively similar and therefore only the results for $k-\omega$ based SST model are presented. Figure 5.5 shows the contour plots of the streamwise and wall-normal mean velocities predicted by $k-\omega$ based SST model. The contours of the streamwise and wall-normal mean velocities are in good agreement with the experimental data.

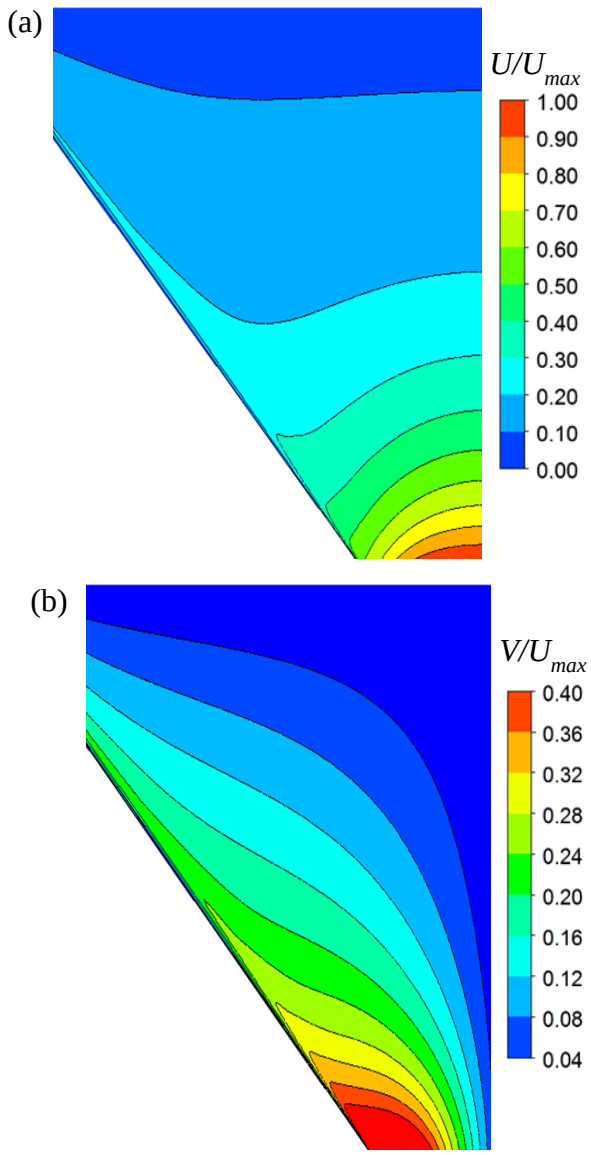

Figure 5.5: Contour plots of streamwise (a) and wall-normal (b) mean velocities for $Re_{d\text{-}53}$ predicted using $k-\omega$ based SST turbulence model.

5.2.2 Profiles of mean velocities

For quantitative assessment of the five different turbulence models in predicting the experimental data, profiles of the mean velocities at selected streamwise locations are examined in this section. The mean velocity profiles are obtained at selected streamwise locations; x/d = 0.8, 1.05, 1.6, 1.9 and 2.1, respectively. An illustration of the profile locations through the hopper, for example, is shown in Figure 5.6. For each profile, the maximum velocity at hopper exit, U_{max} is used to normalize the velocity data.

Figures 5.7, 5.8 and 5.9 compare the prediction and experimental values of the streamwise and wall-normal mean velocities at *x/d* = 0.8, 1.05, 1.6, 1.9 and 2.1. The results indicate that the five different turbulence models used in this study reproduce the correct trends of the mean velocity profiles at all *x/d* locations. Near the inlet of the hopper (*x/d* = 0.8, 1.05 and 1.6) the streamwise mean velocity profiles have a saddle back shape which is correctly predicted by all the turbulence models. However, along the center of the hopper all the turbulence models over predicts the streamwise mean velocity with the prediction improving closer towards the wall. At the same *x/d* locations, the wall-normal mean velocity is under predicted by all the turbulence models. Near the outlet of the hopper (*x/d* = 1.9 and 2.1) the agreement between the experimental and numerical results is good. Overall, the differences between the five different turbulence models for all *x/d* locations are found to be small, less than 5%; however only $k-\omega$ and $k-\omega$ based SST models are able to capture the mean velocities going to zero at the wall. This is because for $k-\omega$ and $k-\omega$ based SST turbulence models in CFX, the computed y^+ value is allowed to fall below 11.06 based on grid refinement and therefore they are able to capture the mean velocities going to zero near the wall. Based on the results, $k-\omega$ based SST model is preferred over $k-\omega$ model for the optimization of hopper geometry as $k-\omega$ based SST model combines the advantages of $k-\varepsilon$ and $k-\omega$ models to give better predictions for contraction flows.

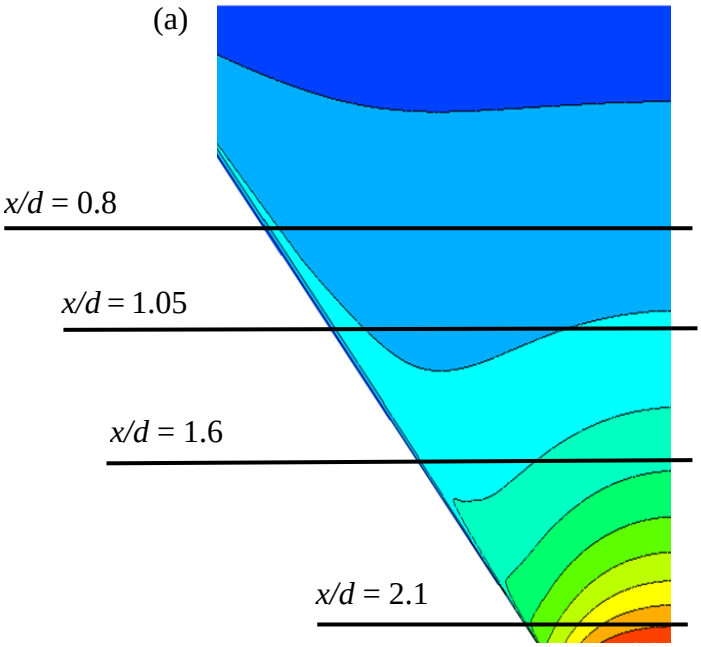

Figure 5.6: Schematic of profile locations for comparison with the experimental data.

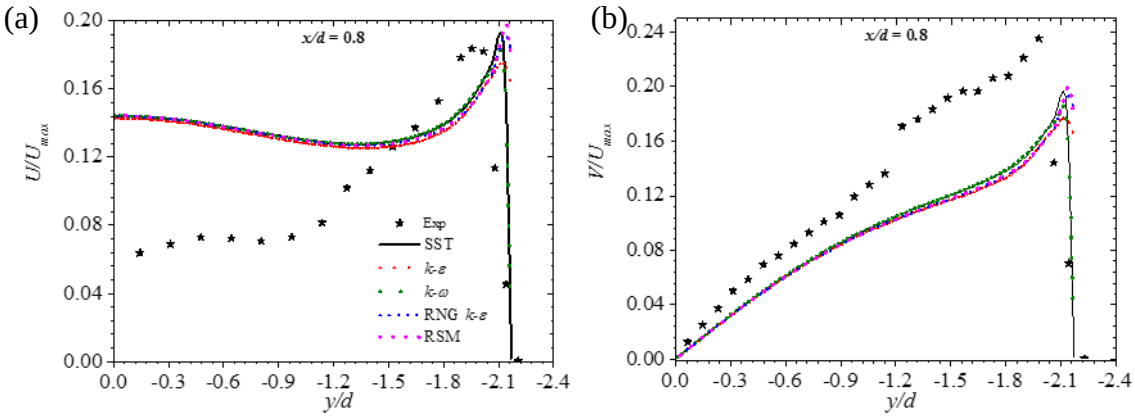

Figure 5.7: Experimental and numerical comparison of streamwise (a) and wall-normal (b) mean velocities at $x/d = 0.8$.

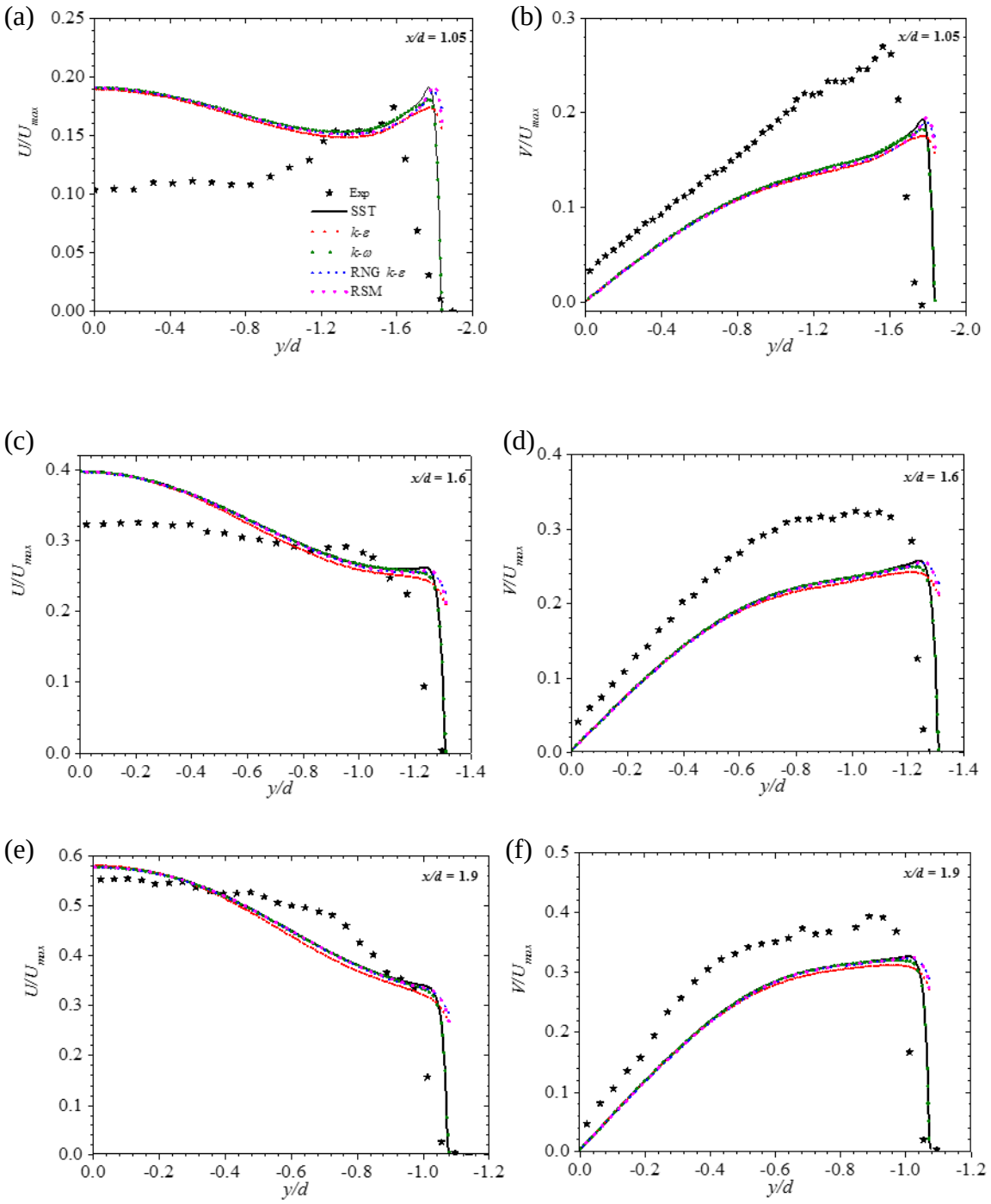

Figure 5.8: Experimental and numerical comparison of streamwise(a);(c);(e) and wall-normal mean velocities (b);(c);(d) at x/d = 1.05 (a),(b); x/d = 1.6 (c),(d); and x/d = 1.9 (e);(f).

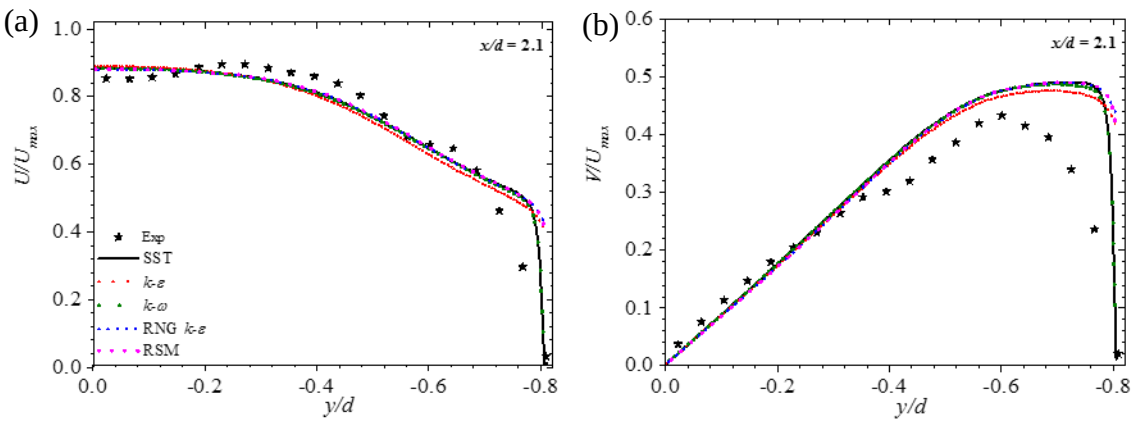

Figure 5.9: Experimental and numerical comparison of streamwise (a) and wall-normal (b) mean velocities at x/d = 2.1.

It should also be noted that when velocity profiles obtained from the experiment are used as inlet boundary condition in CFX, the agreement between the experimental and numerical results are worse compared to mass flow as inlet boundary condition described in chapter 4 because the experimental profiles are obtained only along the center plane and do not include a full sweep at the inlet of the hopper.

Evidence supporting discrepancy between experimental and numerical results through contractions is found in the literature. For example Sanchez et al. (2010), reported that $k-\varepsilon$ turbulence model over predicted the streamwise and wall-normal mean velocities through a sudden contraction which is much simpler than the hopper geometry used in the present study. In the present study, numerical simulations are performed with five different turbulence models ($k-\varepsilon$, RNG $k-\varepsilon$, $k-\omega$, $k-\omega$ based SST and RSM turbulence models) with the intention of reproducing the experimental results. The numerical results for all the turbulence models over predict streamwise mean velocity and under predict wall-normal mean velocity near the hopper inlet.

A possible explanation for the discrepancy between the numerical and experimental results is that the model constants for the turbulence models are not calibrated for the

geometry or flow conditions of the current study since all the turbulence models used in the present study use default model constants in CFX described in chapter 4.

5.3 Optimization of hopper geometry

This section presents the results for the optimization of Refuge One hopper geometry. The optimization parameters include the hopper height (*h*) and wall shape. The dimensions of the hopper for optimization are slightly smaller than the hopper mentioned in Chapter 3 because it is designed for the prototype Refuge One. It has a rectangular inlet which is 471 *mm* long and 273 *mm* wide and transitions into a circular exit with 75 *mm* diameter. This results in a contraction ratio of 29. Three different values are chosen for the first optimization parameter, h = 150 *mm*, 90 *mm* and 60 *mm*, respectively. These values are chosen based on the maximum available space in the prototype Refuge One.

5.3.1 Wall shapes

For the second optimization parameter, two contraction wall shapes are chosen based on the wind tunnel contraction studies by Morel (1975) and Sargison et al. (2004) in order to avoid flow separation. For each of the hopper heights, wall shapes are generated based on the equations of Morel (1975) and Sargison et al. (2004). A Tapered wall shape similar to the hopper described in Chapter 3 is also selected for comparison.

Equations (5.1) and (5.2) show the variables that are used to define Morel (1975)'s wall shapes, where D_1 and D_2 are the inlet and exit diameters, x_i is the inflection point where the two equations intersect, D is the loci of the wall shape along the wall-normal axis, x is the distance along x axis and h is the height of the contraction. For the present work, the equations used by Morel (1975) are modified to a hopper with a rectangular cross section. The diameters D_1 and D_2 in the equations are replaced with the width and height

of the hopper to obtain two different equations defining the vertical and horizontal wall shapes. The inflection point (x_i) is placed at $0.5h$ based on the data provided by Morel (1975).

$$\frac{D-D_2}{D_1-D_2} = 1 - \frac{\left(\frac{x}{h}\right)^3}{\left(\frac{x_i}{h}\right)^2} \text{ for } 0 \leq \frac{x}{h} \leq \frac{x_i}{h} \tag{5.1}$$

$$\frac{D-D_2}{D_1-D_2} = \frac{\left(1-\frac{x}{h}\right)^3}{\left(1-\frac{x_i}{h}\right)^2} \text{ for } \frac{x_i}{h} \leq \frac{x}{h} \leq 1 \tag{5.2}$$

Equation (5.3) shows the variables that are used to define the wall shape proposed by Sargison et al. (2004), where y is the loci of the wall shape, x is the distance along streamwise direction and a-g are contraction parameters as defined by Sargison et al. (2004).

$$y = ax^6 + bx^5 + cx^4 + dx^3 + ex^2 + fx + g \tag{5.3}$$

5.3.2 Test conditions

The test conditions for optimization of hopper geometry are summarized in Table 5.1. The test conditions for the Tapered hoppers are denoted by H_iT where H represents the height of the hopper (i = 60 *mm*, 90 *mm* and 150 *mm*) and T represents Tapered wall shape. Similarly, the test conditions for Sargison's and Morel's hoppers are denoted by H_iS and H_iM where S and M represents Sargison's and Morel's wall shapes. A total of nine configurations of heights and wall shapes are generated. For all the tests, flow rate of 0.0396 m^3/s is used. This flow rate is based on the operating conditions of the prototype Refuge One. For the numerical simulations, a corresponding mass flow of $\dot{m}$ = 0.034 *kg/s* is set as the inlet boundary condition. All other boundary conditions are similar to those described in Chapter 4. The simulations are performed with $k-\omega$

based SST turbulence model as discussed in Section 5.2. From here on, the hoppers designed using Tapered wall shape will be referred to as Tapered hoppers, hoppers designed using Morel (1975)'s wall shape will be referred to as Morel's hoppers and hoppers designed using Sargison et al. (2004)'s wall shape will be referred to as the Sargison's hoppers for ease of use.

Table 5.1: Summary of test conditions for optimization of hopper

Test condition	Hopper height (*mm*)	Wall shape
$H_{150}T$	150	Tapered
$H_{150}M$	150	Morel
$H_{150}S$	150	Sargison
$H_{90}T$	90	Tapered
$H_{90}M$	90	Morel
$H_{90}S$	90	Sargison
$H_{60}T$	60	Tapered
$H_{60}M$	60	Morel
$H_{60}S$	60	Sargison

5.3.3 Grid independent tests

Grid independent tests are conducted for the nine test conditions using 4 computational grids: 1,235,295 elements (gird A), 2,180,646 elements (grid B), 4,031,428 elements (grid C) and 6,165,376 elements (grid D), respectively. Table 5.2 shows the grid independence test results for the Tapered hoppers. Based on the results, grid C is chosen for the optimization of Tapered hoppers. Grid independent tests are also conducted for Sargison's and Morel's hoppers and similar results are observed. Therefore, grid C is also chosen for the optimization of Sargison's and Morel's hoppers.

Table 5.2: Grid independence test results for maximum percentage differences between four grids (grids A-D) for area averaged streamwise mean velocity at hopper exit, streamwise and wall-normal mean velocity profiles at two locations (x/h = 0.5 and 1) and area averaged pressure difference between the inlet and exit for Tapered hopper

Grids	Streamwise velocity at hopper exit	Streamwise velocity at *x/H*		Wall-normal velocity at *x/H*		Pressure difference
		0.5	**1**	**0.5**	**1**	
A and B	-0.34%	-2.41%	-7.30%	-2.22%	2.09%	1.42%
B and C	-0.04%	-1.54%	-1.59%	-2.59%	1.08%	0.50%
C and D	-0.01%	-0.07%	-0.07%	-1.02%	0.07%	0.05%

5.3.4 Optimization results

5.3.4.1 Contour plots of mean velocities

This section shows the contour plots of streamwise and wall-normal mean velocities along the center plane (*x*-*y*) for the nine hopper configurations. The contour plots of streamwise and wall-normal mean velocities are presented to visualize the effect of contraction height and wall shape on the flow pattern. The contour plots are normalized by the centerline streamwise velocity at hopper exit, U_{exit}.

Figures 5.10, 5.11 and 5.12 show the contour plots of streamwise mean velocities for the three hopper heights designed using Tapered, Sargison's and Morel's methods. For

each test condition, the contours of the streamwise velocities show flow acceleration along the streamwise distance. This is expected because of favourable pressure gradient caused by the contraction. As a result of strong favourable pressure gradient, none of the hoppers show flow separation as indicated by the contours. The contours of streamwise mean velocities are qualitatively similar for all the hopper test conditions, however on a closer look the contours are identical for Sargison's and Morel's hoppers which have curved wall shapes in comparison to Tapered hoppers which have a straight wall shape. Irrespective of the hopper height, Tapered hoppers have the maximum streamwise velocity and Morel's hoppers have the minimum streamwise velocity at the hopper exit. The maximum streamwise velocity for $H_{150}T$, where subscript 150 refers to hopper height and T refers to Tapered wall profile (see) , is 14.7% and 16.8% higher than $H_{150}S$ and $H_{150}M$ where S and M refer to Sargison's and Morel's wall profiles. The contours also show that the maximum velocity increases with decreasing hopper height. The streamwise velocity increases by 11.9% for Tapered hoppers, 24.6% for Sargison's hoppers and 25.2% for Morel's hoppers as the hopper height decreases from 150 *mm* to 60 *mm*. The contours also show that Tapered hopper of height 60 *mm* ($H_{60}T$) has the maximum velocity and Morel's hopper of height 150 *mm* ($H_{150}M$) has the minimum velocity among all the test conditions. The results indicate that in terms of the maximum velocity, both the choice of hopper wall and height combine to augment the effect produced by one another.

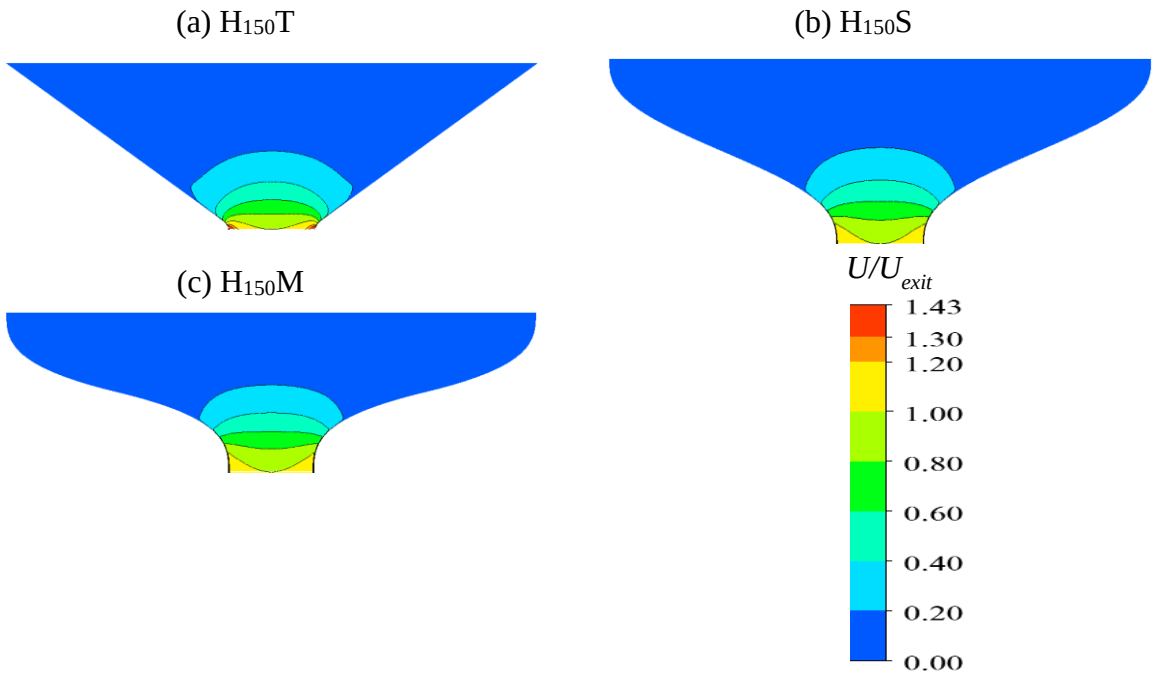

Figure 5.10: Contour plots of streamwise mean velocities for hoppers designed using Tapered (a) Sargison's (b) and Morel's (c) methods for contraction height 150 *mm*.

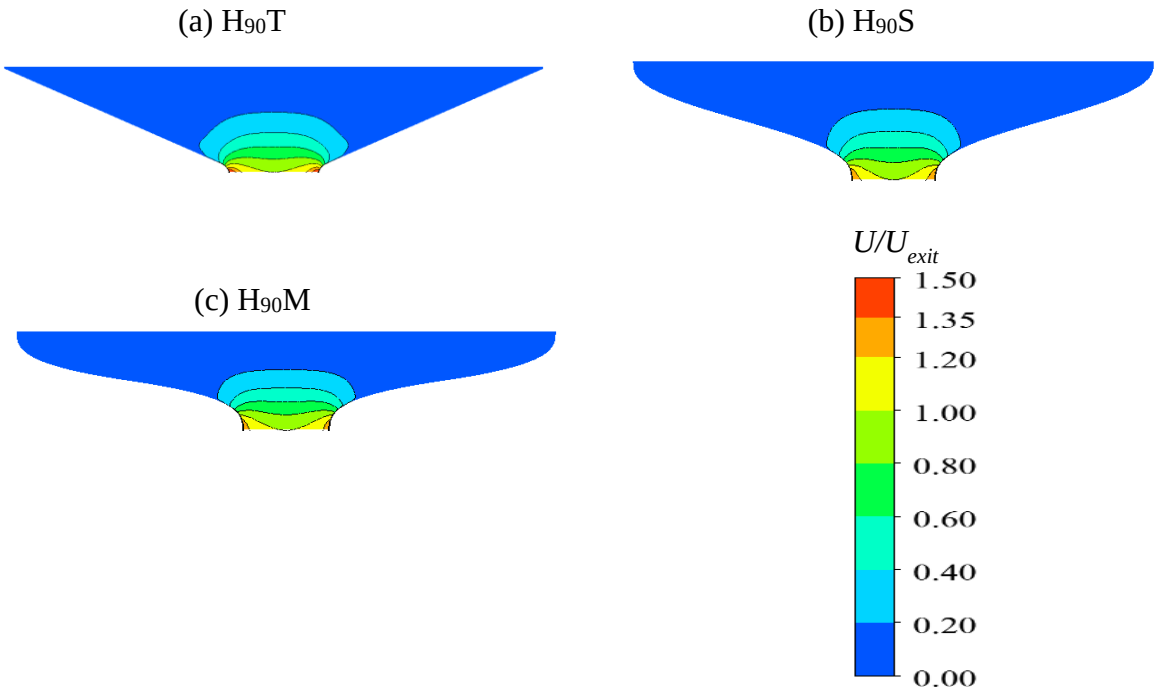

Figure 5.11: Contour plots of streamwise mean velocities for hoppers designed using Tapered (a) Sargison's (b) and Morel's (c) methods for contraction height 90 *mm*.

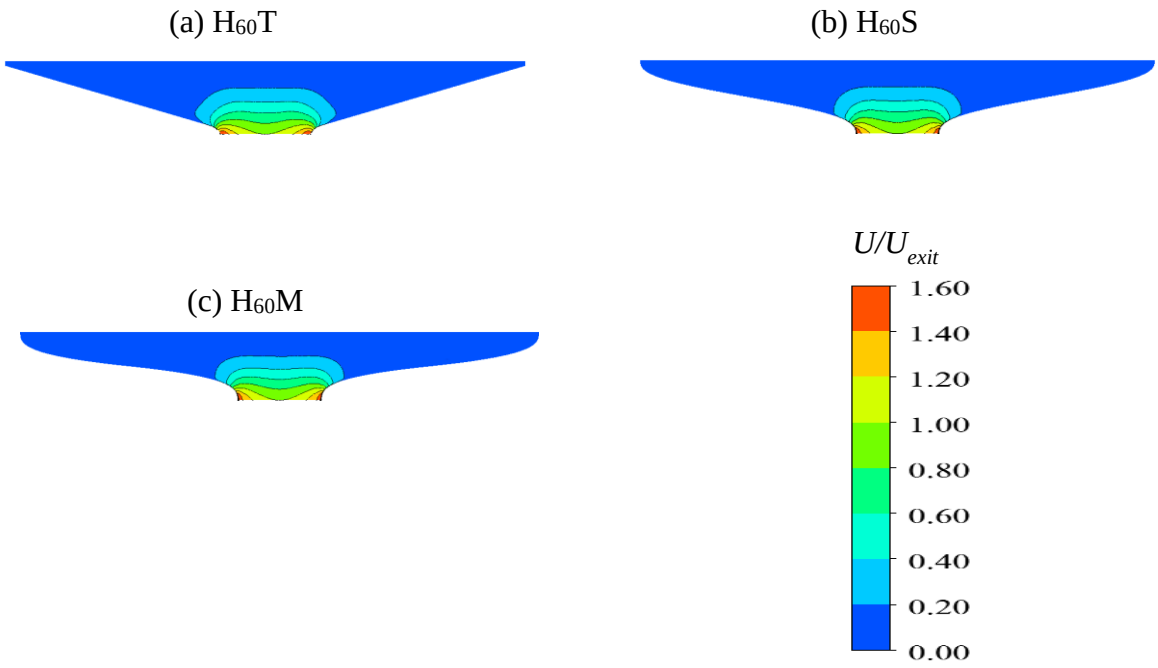

Figure 5.12: Contour plots of streamwise mean velocities for hoppers designed using Tapered (a) Sargison's (b) and Morel's (c) methods for contraction height 60 *mm*.

Figures 5.13, 5.14, 5.15 show the contour plots of wall-normal mean velocities for the three hopper heights designed using Tapered, Sargison's and Morel's methods. The contours display positive velocities on one side, negative velocities on the opposite side and zero velocity along the center of the hopper. The positive and negative wall-normal mean velocities are indications that gradual contraction of the hopper causes flow from opposite sides to move towards each other and converge along the center of the hopper. The increase in wall-normal mean velocities along the streamwise distance can be attributed to the favourable pressure gradient. Among the three wall shapes, the maximum velocity is obtained for Tapered hoppers and minimum velocity is obtained for Morel's hoppers. The contours also show that as the height of the hopper is reduced the effect of wall shapes on maximum wall-normal velocity becomes less significant. The maximum velocity for Tapered hopper of height 150 *mm* ($H_{150}T$) is 38.7% and 44% higher than Sagison's ($H_{150}S$) and Morel's ($H_{150}M$) hoppers of the same height whereas for Tapered hopper of height 60 *mm* ($H_{60}T$) the maximum velocity is only

12.7% and 19.1% higher than Sagison's ($H_{60}S$) and Morel's ($H_{60}M$) hoppers of the same height.

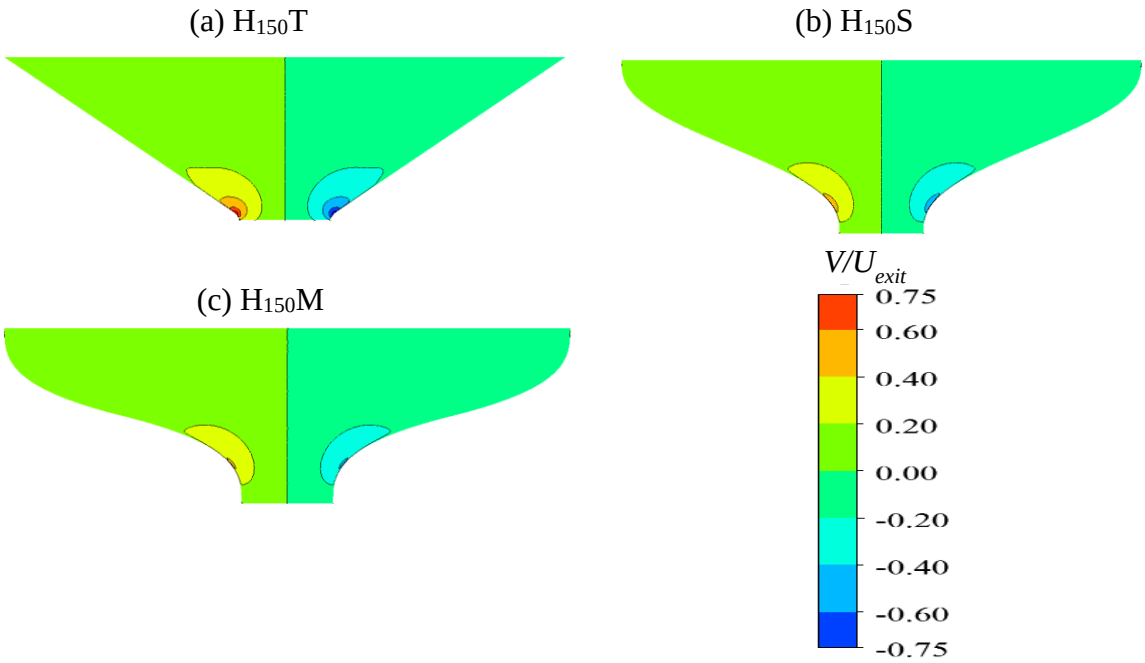

Figure 5.13: Contour plots of wall-normal mean velocities for hoppers designed using Tapered (a) Sargison's (b) and Morel's (c) methods for contraction height 150 *mm*.

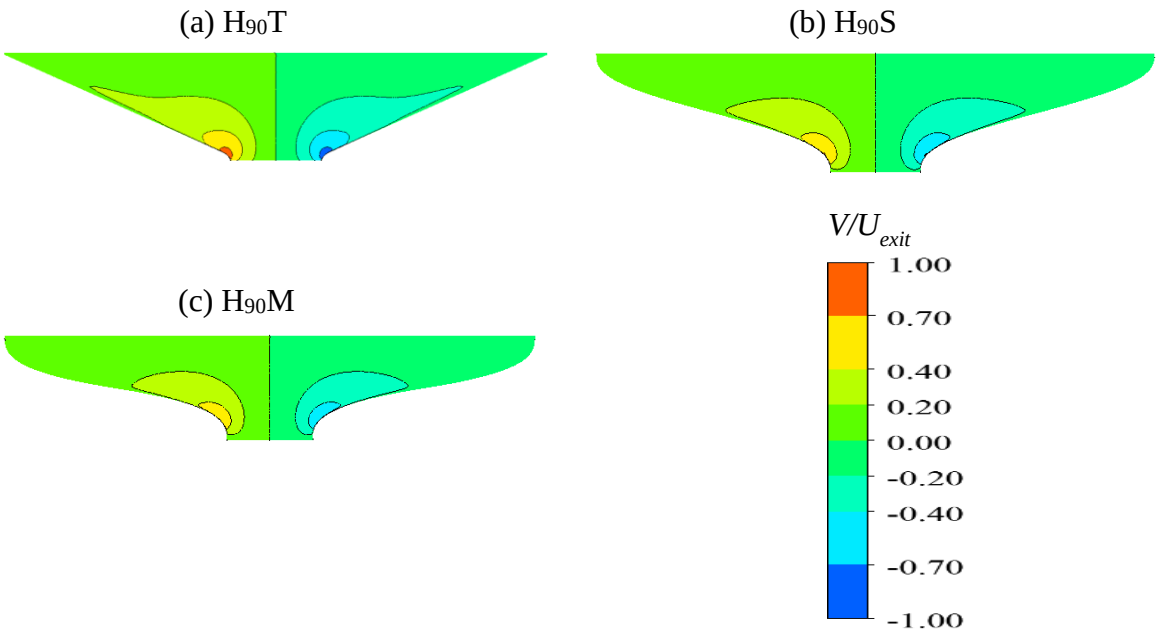

Figure 5.14: Contour plots of wall-normal mean velocities for hoppers designed using Tapered (a) Sargison's (b) and Morel's (c) methods for contraction height 90 *mm*.

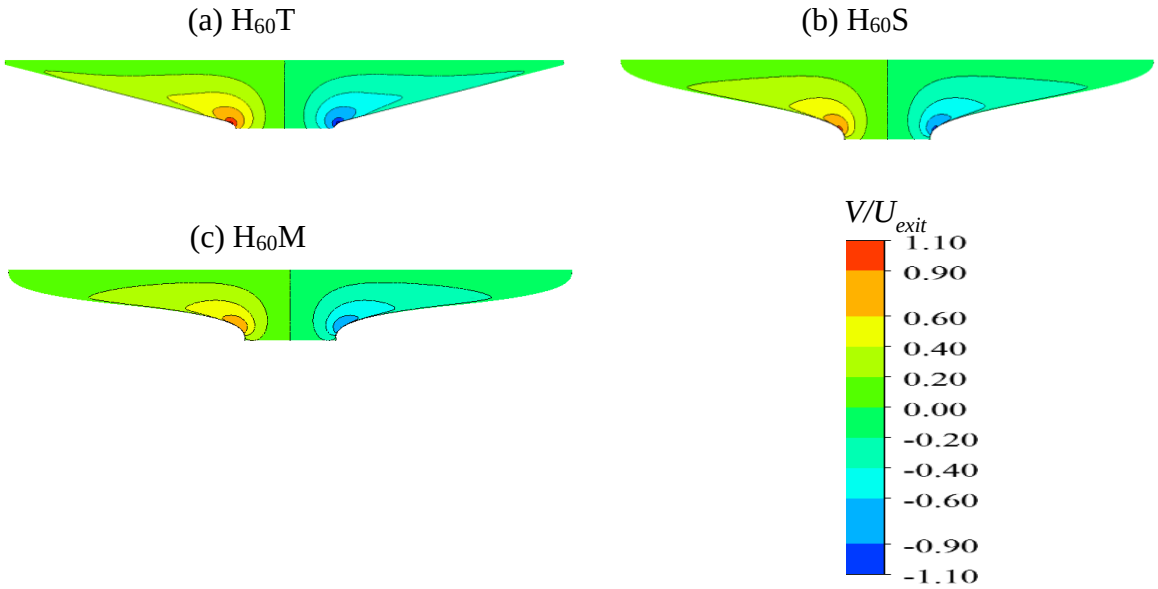

Figure 5.15: Contour plots of wall-normal mean velocities for hoppers designed using Tapered (a) Sargison's (b) and Morel's (c) methods for contraction height 60 *mm*.

The contours of streamwise mean velocities at the cross sectional exit plane ($x/h = 1$) are presented to show the effect of hopper wall shape and height on velocity non uniformity. Velocity non uniformity is defined as the deviation between the maximum streamwise velocity and the centerline streamwise velocity at the hopper exit. Figure 5.16 shows the contours of streamwise mean velocities at the exit plane for hopper height 150 *mm* with different wall shapes in order to study the effect of wall shape on velocity non uniformity. Figures 5.17 and 5.18, show the contours of streamwise mean velocities for hopper heights 90 *mm* and 60 *mm*, respectively. At the hopper exit ($x/h = 1$), the contours reveal that maximum velocity occurs close to the hopper walls. The contours also show that Tapered hoppers have the highest and Morel's hoppers have the lowest velocity non uniformity. This implies that the core flow for Morel's hoppers is less affected by maximum velocity compared to Tapered hoppers. The velocity non uniformity at the hopper exit increases for decreasing hopper height. This is expected since the wall curvature at the hopper exit increases which increases the velocity non uniformity for shorter hopper heights. The results also show that the influence of decreasing height is felt more strongly for Morel's hoppers even though it has the least velocity non uniformity.

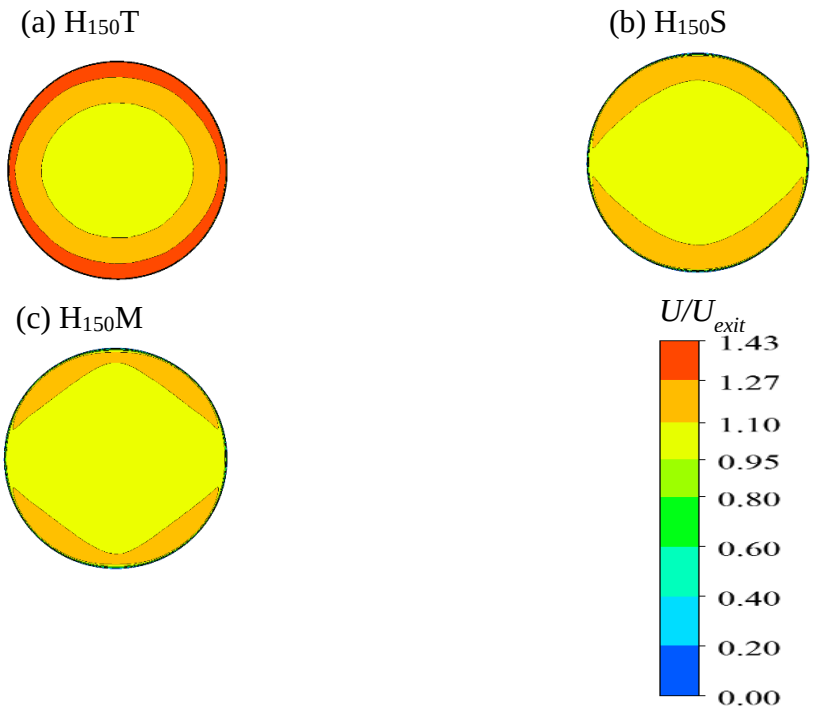

Figure 5.16: Contour plots of streamwise mean velocities at exit plane for hoppers designed using Tapered (a) Sargison's (b) and Morel's (c) methods for contraction height 150 *mm*.

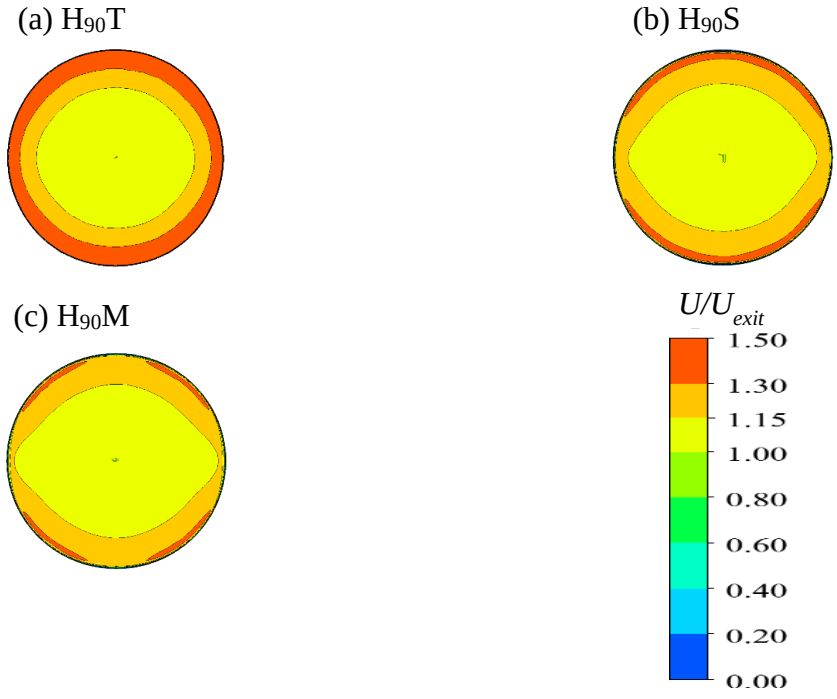

Figure 5.17: Contour plots of streamwise mean velocities at exit plane for hoppers designed using Tapered (a) Sargison's (b) and Morel's (c) methods for contraction height 90 *mm*.

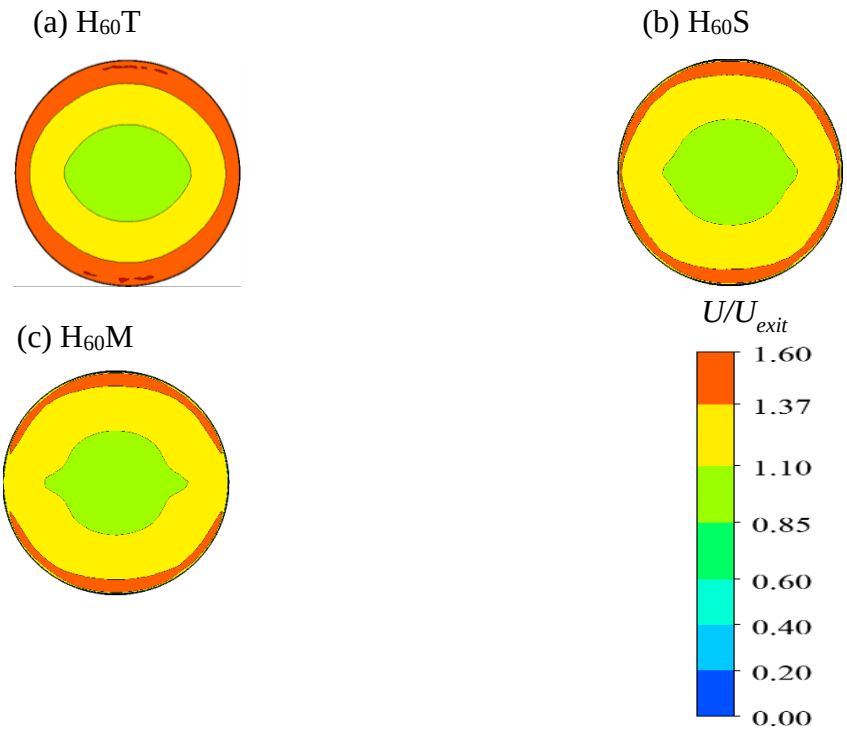

Figure 5.18: Contour plots of streamwise mean velocities at exit plane for hoppers designed using Tapered (a) Sargison's (b) and Morel's (c) methods for contraction height 60 *mm*.

5.3.4.2 Contour plots of pressure coefficient

Since the flow is accelerated through the contraction, strong favourable pressure gradient is formed in the hopper, as would be expected. However, there can be localized regions of adverse pressure gradient near the hopper inlet and outlet depending on the hopper wall shape and height. In this section, the contour plots of pressure coefficient are used to study the effect of hopper wall shape and height on the pressure distribution. The coefficient of pressure, C_p, is defined as:

$$C_p = \frac{(p - p_{exit})}{{}^1/_2 \rho {U_{exit}}^2} \tag{5.4}$$

where p is the local pressure, p_{exit} is the centerline pressure at hopper exit, ρ is the density of air and U_{exit} is the centerline streamwise velocity at hopper exit.

The distribution of C_p for all the nine hopper configurations is presented in Figures 5.19, 5.20 and 5.21. The contours reveal the presence of strong favourable pressure gradient caused by the contraction which is expected. Adverse pressure gradient near the hopper inlet and exit is not observed for any of the hopper designs. The largest pressure gradient occurs near the corners, and thus, the maximum velocity also occurs near the corners. The effect of hopper wall shape on the pressure distribution for h = 150 *mm* is shown in Figure 5.19. The contours of the pressure distribution are qualitatively similar for all the three wall shapes, however the contours show the strong effect that varying wall shape has on the C_p extrema near the corners. The C_p minimum near the corners for Tapered hopper of height 150 *mm* is nearly 60% and 65% larger than Sargison's and Morel's hoppers. The C_p extrema is also sensitive to hopper height. For decreasing hopper height the minimum pressure significantly increases for all the wall shapes. The C_p extrema near the hopper outlet also indicates the location where the flow separation probability is the most. This means that the hopper with least C_p extrema near the outlet is desirable to avoid any possibility of flow separation.

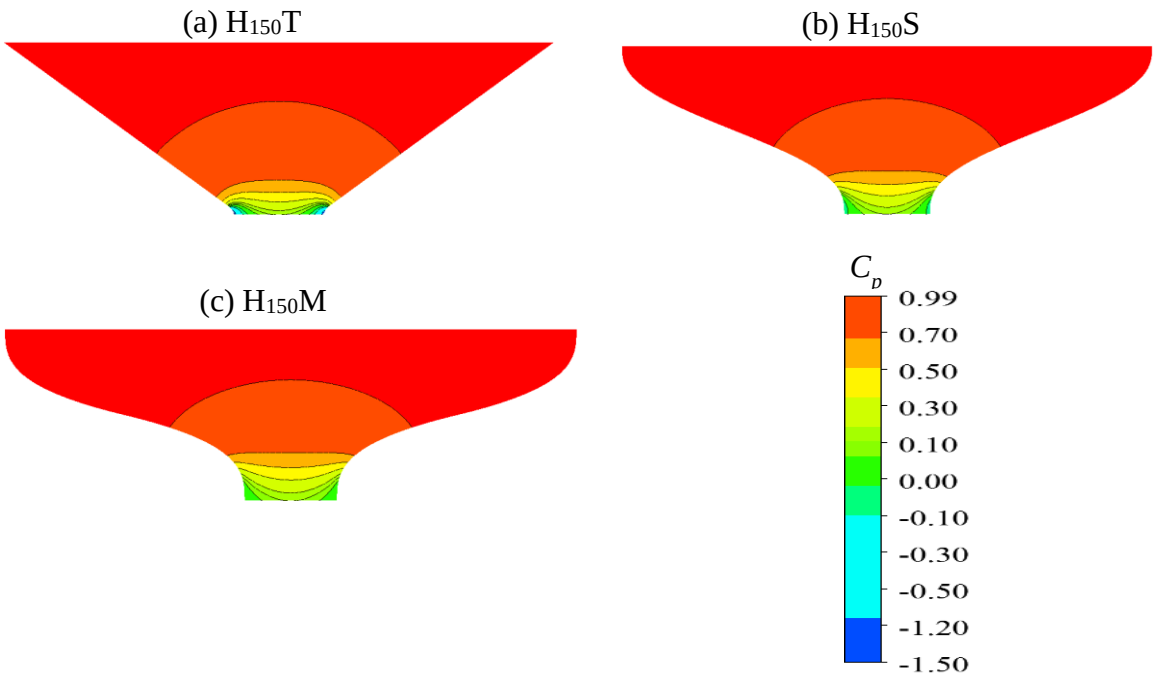

Figure 5.19: Contour plots of pressure coefficient for hoppers designed using Tapered (a) Sargison's (b) and Morel's (c) methods for contraction height 150 *mm*.

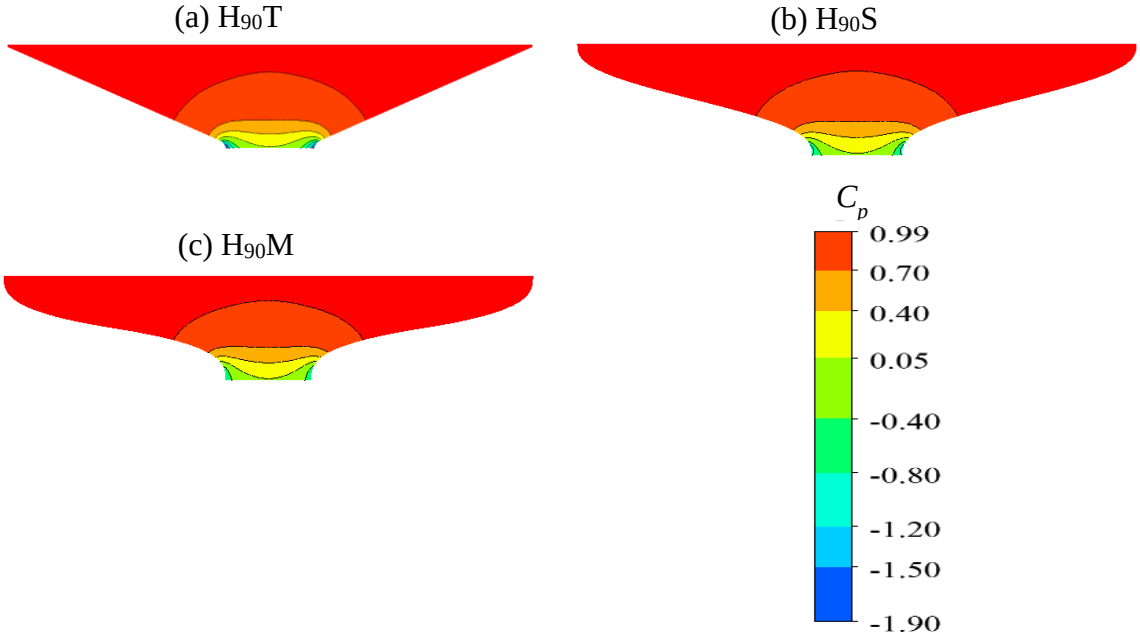

Figure 5.20: Contour plots of pressure coefficient for hoppers designed using Tapered (a) Sargison's (b) and Morel's (c) methods for contraction height 90 *mm*.

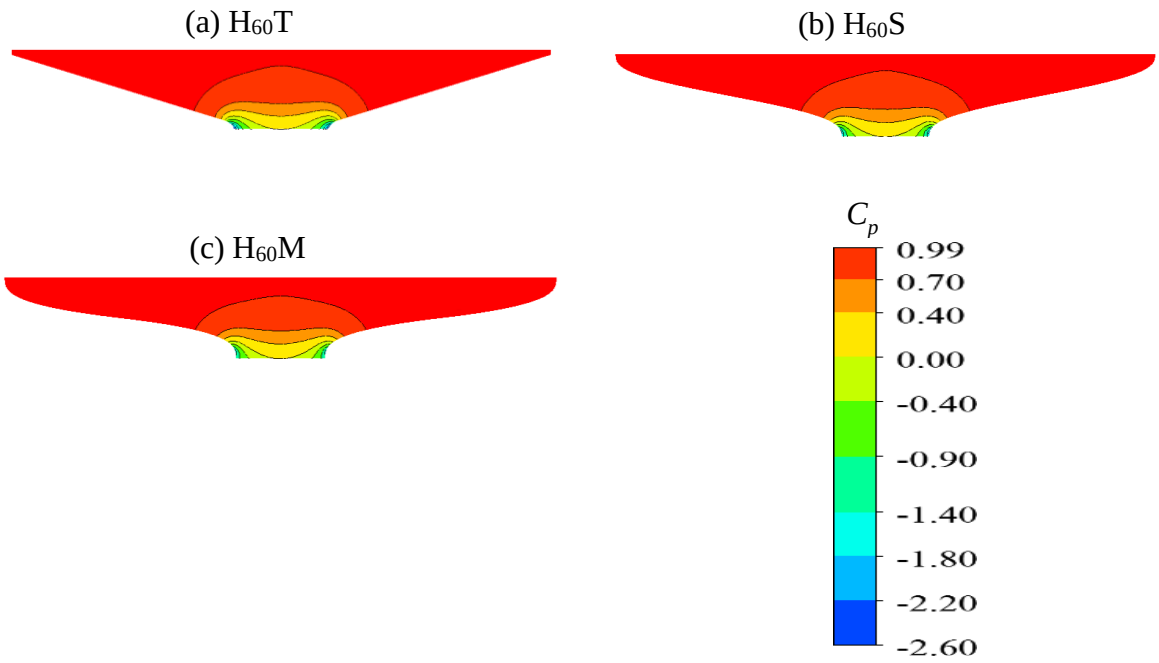

Figure 5.21: Contour plots of pressure coefficient for hoppers designed using Tapered (a) Sargison's (b) and Morel's (c) methods for contraction height 60 *mm*.

5.3.4.3 Contour plots of skin friction coefficient

In this section, the contours of skin friction coefficient (C_f) are presented to visualize the effect of hopper wall shape and height on the wall shear stress for different hopper configurations. The contours of C_f are also used to indicate if the flow separates through the hopper. The contours are obtained along the center plane for all the hopper configurations. The C_f is defined using the following relationship:

$$C_f = \frac{\tau_w}{{}^1/_2 \rho {U_{exit}}^2} \tag{5.4}$$

where τ_w is the wall shear stress, ρ is the density of air and U_{exit} is the centerline streamwise velocity at hopper exit.

The effects of hopper wall shape and height on the skin friction coefficient are depicted in Figures 5.22, 5.23 and 5.24, respectively. The C_f remains positive all through the hopper, thus indicating that there is no separation for any of the hopper designs. Among

the wall shapes, Tapered hoppers have the highest C_f and Morel's hoppers have the lowest C_f. For shorter hopper heights, C_f increases for all the wall shapes, however the increase in C_f varies for different wall shapes. It is found that C_f for Tapered hoppers are least affected by changes in hopper height whereas for Sargison's and Morel's hoppers the C_f are significantly affected by changes in hopper height.

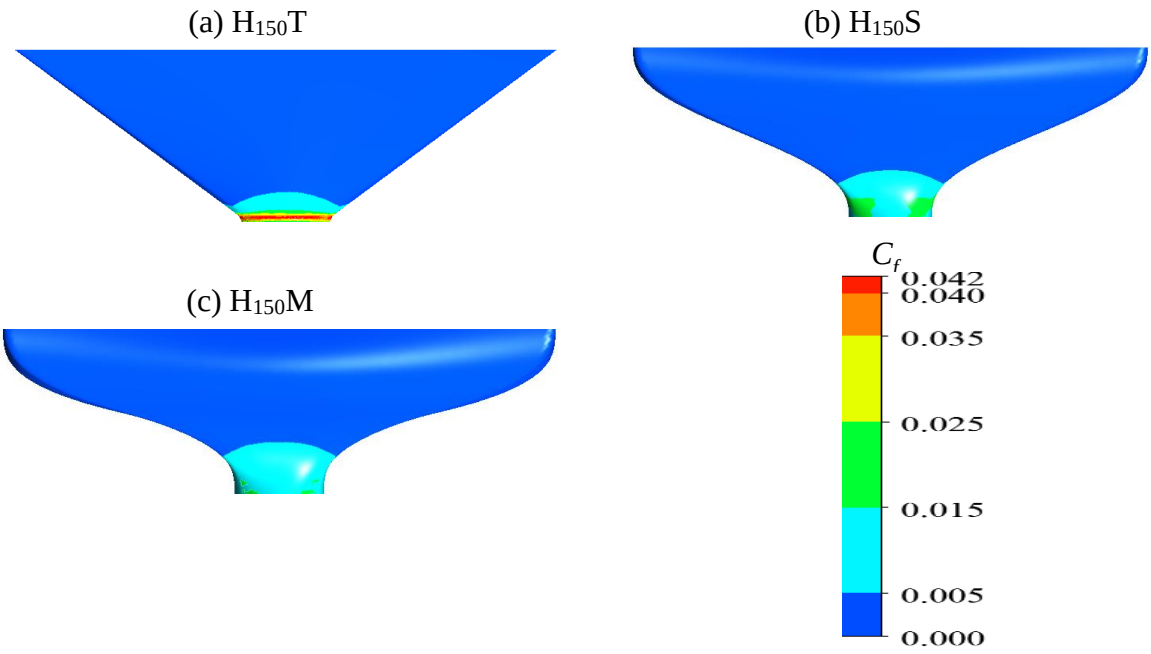

Figure 5.22: Contour plots of skin friction coefficient for hoppers designed using Tapered (a) Sargison's (b) and Morel's (c) methods for contraction height 150 *mm*.

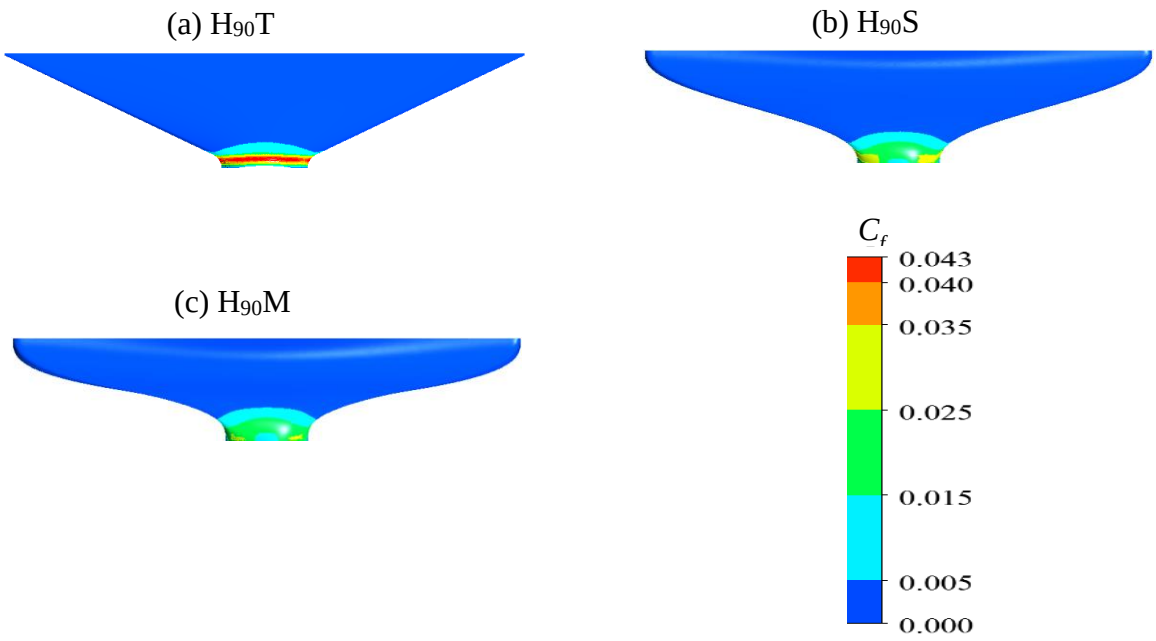

Figure 5.23: Contour plots of skin friction coefficient for hoppers designed using Tapered (a) Sargison's (b) and Morel's (c) methods for contraction height 90 *mm*.

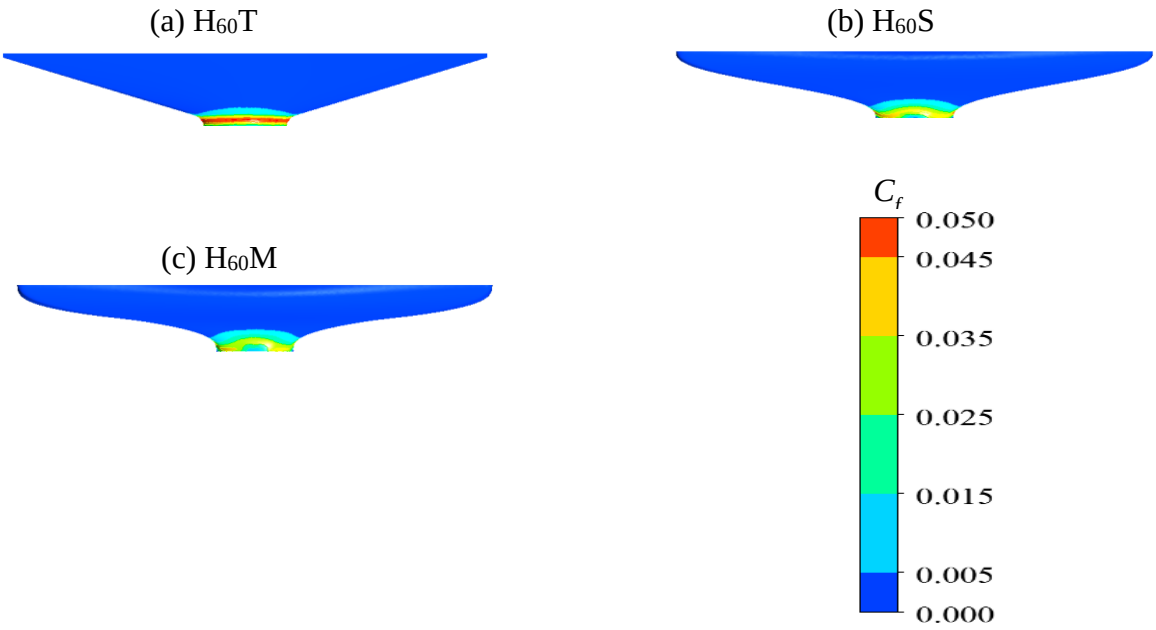

Figure 5.24: Contour plots of skin friction coefficient for hoppers designed using Tapered (a) Sargison's (b) and Morel's (c) methods for contraction height 60 *mm*.

5.3.4.4 Profile plots of streamwise mean velocities, pressure and skin friction coefficient

To quantify the effect of hopper height and wall shape on the streamwise mean velocity, pressure and skin friction coefficient, profiles along the hopper centerline and wall are examined in this section. For the velocity profiles, the centerline streamwise mean velocity at hopper exit, U_{exit} is used as the velocity scale. The streamwise distance is normalized by the corresponding hopper height, h for each profile.

Figure 5.25 shows that the streamwise mean velocity along the centerline for all the hopper test conditions remains nearly constant from the inlet until $x/h = 0.1$. This is followed by a rapid increase through the hopper. The centerline velocities for Sargison's and Morel's hoppers have slight differences between them as the velocity increase is slightly delayed for Sargison's hoppers because of differences in wall shapes. However, the centerline velocity for Tapered hoppers is significantly delayed, followed by a sharper rise. This is due to the fact that Tapered hoppers have a straight wall shape which results in a smaller cross sectional area, hence the greatest velocity increase along the centerline. As the hopper height is reduced, the Tapered, Sargison's and Morel's hoppers all exhibit similar increase in streamwise mean velocity along the centerline.

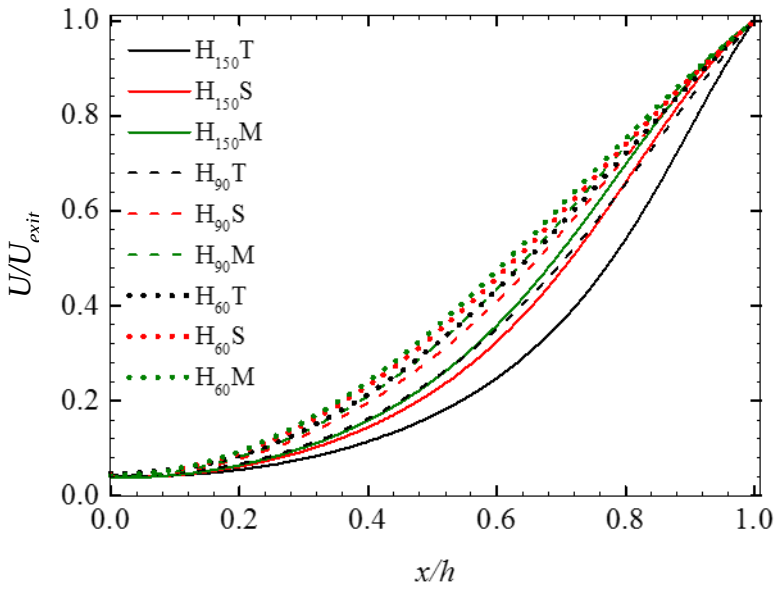

Figure 5.25: Comparison of streamwise mean velocities along hopper centerline for the three hopper heights (h = 150 *mm*, 90 *mm* and 60 *mm*) designed using Tapered, Sargison's and Morel's methods.

Figure 5.26 shows the pressure distribution along the hopper centerline for the Tapered, Sargison's and Morel's hoppers. For each hopper test condition, the effect of favourable pressure gradient causes the pressure to decrease along the streamwise distance. As the flow passes through the hopper, the effect of favourable pressure gradient increases and the C_p profiles gradually decrease along the center line from the maximum at the hopper inlet to minimum at the hopper exit (x/h = 1). The location of C_p minimum corresponds to the location of maximum streamwise mean velocity. The trend of C_p agrees with the profiles of the streamwise mean velocity along the center line. The pressure drop however, depends on the hopper shape and height. Among the three wall shapes, Tapered hoppers have the highest pressure drop while Morel's hoppers have the least pressure drop. As the hopper height decreases the pressure drop also decreases for all the wall shapes, however the effect of wall shape on pressure drop becomes less significant for shorter heights.

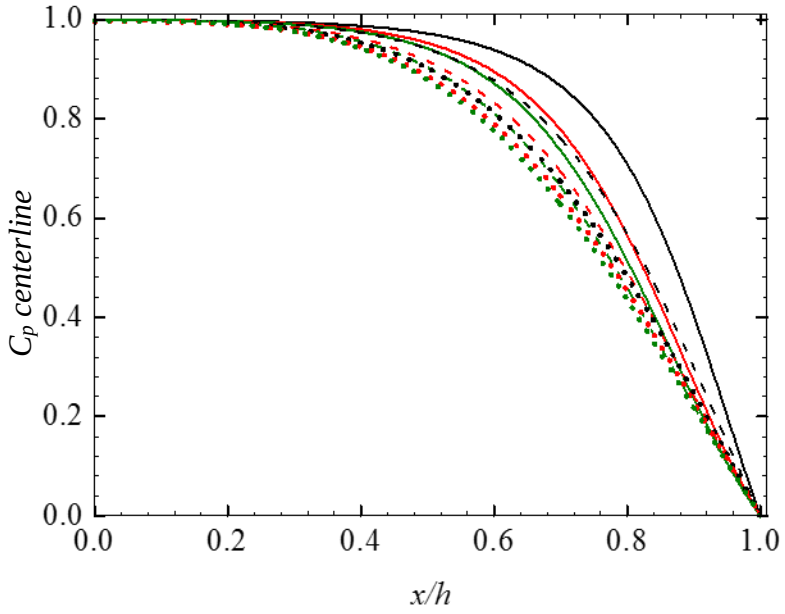

Figure 5.26: Comparison of pressure coefficient along hopper centerline for the three hopper heights (h = 150 *mm*, 90 *mm* and 60 *mm*) designed using Tapered, Sargison's and Morel's methods.

The pressure distribution along the hopper walls is presented in Figure 5.27. For a contraction of finite length, there exists two locations (one near the inlet and one near the outlet) where pressure extremes exist and due to this the possibility of flow separation is of considerable concern. This phenomenon occurs because the wall suddenly changes from curved to a flat region which causes localized pressure extremes. The pressure coefficient profiles, shown in Figure 5.27, are characterized by a steady decline in C_p till x/h = 0.6 before falling to a minimum value near the hopper exit. A short region of adverse pressure gradient follows the C_p minimum near the exit. There is also a region of pressure extrema near the hopper inlet, but its effect is subtle and not visible from the wall C_p profiles. The hopper wall shapes, however have a dramatic effect on the pressure extrema near the hopper exit. As the wall curvature near the hopper exit decreases, the pressure extrema and adverse pressure gradient are also expected to decrease which are indicated by the profiles. For Tapered hoppers the C_p extrema and the adverse pressure gradient at exit are significantly larger than all the

other hopper wall shapes. However, as the wall curvature near the exit decreases the C_p extrema also decreases for Sargison's and Morel's hoppers compared to Tapered hopper. Also, for Sargison's and Morel's hoppers the location of C_p minimum is placed slightly away from the contraction exit as they have a smoother transition from a curved to a straight region compared to Tapered hoppers. The least C_p extrema is obtained for Morel's hoppers as they have a slightly smoother wall curvature compared to Sargison's hoppers. Previous studies also show that contraction shape affects the localized pressure gradient near the inlet and exit of contractions and the shape may be varied to obtain the desired results depending on their application (Watmuff, 1986; Bell and Mehta, 1989).

Figure 5.27 also shows the effect of hopper height on wall pressure distribution. Irrespective of wall shapes, C_p extrema near the exit is enhanced when the hopper height is reduced. Shorter heights are desirable for savings in space and cost, however the risk of flow separation increases as the height is reduced. Among the three wall shapes, Morel's hoppers exhibit the greatest increase in C_p extrema and Tapered hoppers show the least increase in C_p extrema as the height is reduced. Also, for shorter heights the pressure extrema at the inlet increases. For hoppers with height 150 *mm*, the C_p near the inlet is nearly 1, however as the height decreases the C_p increases by 14% and 31% for h = 90 *mm* and 60 *mm*, respectively.

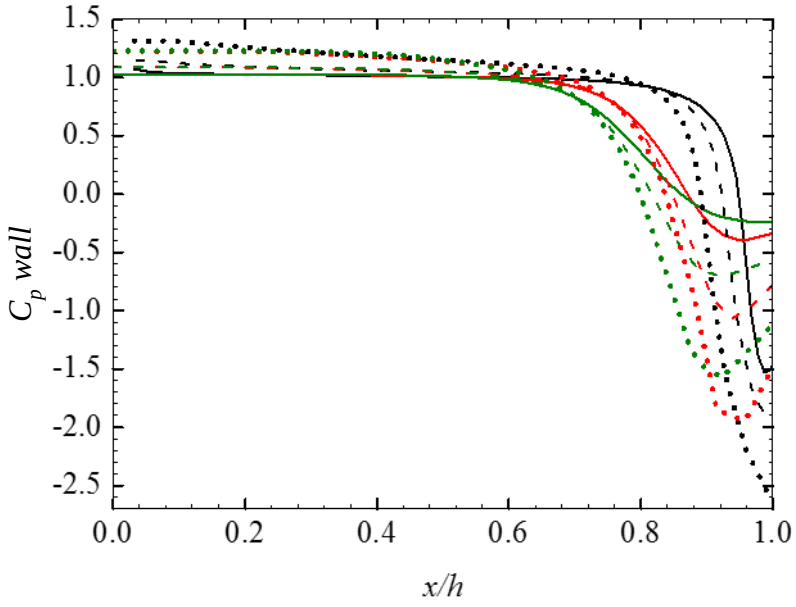

Figure 5.27: Comparison of pressure coefficient along hopper wall for the three hopper heights (h = 150 *mm*, 90 *mm* and 60 *mm*) designed using Tapered, Sargison's and Morel's methods.

Figure 5.28 shows the skin friction coefficient for the three hopper heights designed using Tapered, Sargison's and Morel's methods. The C_f increases through the hopper caused by the passage of the flow through a strong favourable pressure gradient. For all the hopper test conditions, the C_f distribution clearly shows that flow separation is not expected since C_f remains positive throughout the contraction. The maximum C_f is observed for Tapered hoppers and the minimum C_f is observed for Morel's hoppers. The location of C_f maximum shifts further inside the hopper exit for Sargison's and Morel's hoppers because they have a smoother wall transition at the exit. As the hopper height decreases the C_f increases for all the wall shapes, however the C_f difference between the wall shapes diminishes for shorter hopper heights.

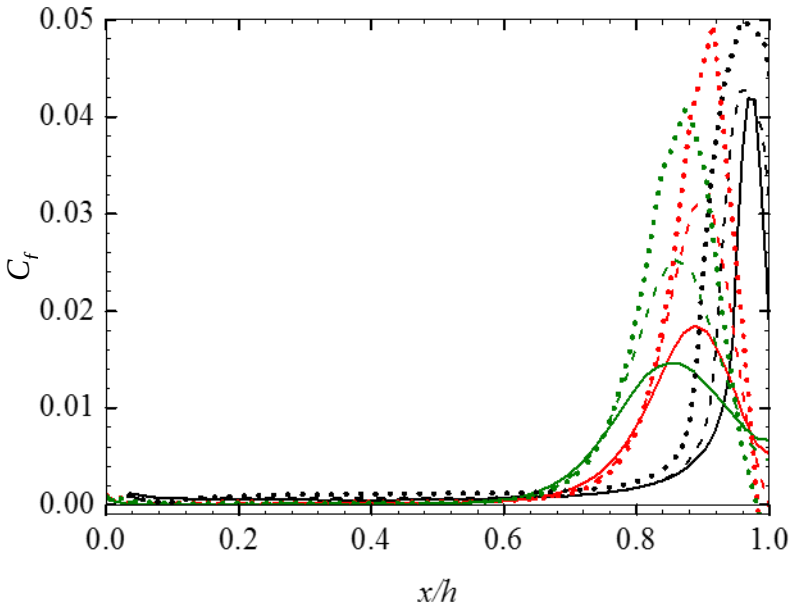

Figure 5.28: Comparison of skin friction coefficient along hopper wall for the three hopper heights (h = 150 *mm*, 90 *mm* and 60 *mm*) designed using Tapered, Sargison's and Morel's methods.

5.3.4.5 Comparison of head loss

In this section the effect of hopper wall shape and height on the head loss is presented in order to choose the optimum hopper design that would yield minimum head loss. Equation (5.5) is a convenient way of writing modified Bernoulli equation to include the difference in static and dynamic pressure and hopper height equated to the head loss. The head loss is shown below.

$$\Delta H = \left(\frac{p_1}{\rho g} + \frac{v_1^2}{2g} + h_1\right) - \left(\frac{p_2}{\rho g} + \frac{v_2^2}{2g} + h_2\right) \tag{5.5}$$

where p_1 is the area averaged pressure at inlet, v_1 is the area averaged velocity at inlet, p_2 is the area averaged pressure at hopper exit (x/h = 1), v_2 is the is the area averaged velocity at hopper exit, ρ is the density of air, g is the acceleration due to gravity and $(h_1 - h_2)$ is the hopper height.

When the fluid passes through the hopper, the velocity of the flow will increase at the region of smallest cross sectional area and consequently the static pressure will decrease. There will be dissipation of energy through the hopper as some of the static pressure drop converts into kinetic energy and head loss or total pressure loss. Figure 5.29 shows the comparison of head loss for the three hopper heights designed using Tapered, Sargison's and Morel's methods. The head loss is very much dependent on hopper wall shape and height. Among the wall shapes, the head losses for Sargison's and Morel's hoppers are smaller than Tapered hoppers. This can be attributed to a smoother wall transition which reduces the pressure drop for Sargison's and Morel's hoppers. For shorter hopper heights, the head loss increases however, the choice of wall shape has a significant effect on the percentage increase in head loss. On the contrary, for hopper height 90 *mm*, the head loss for Morel's hopper decreases in spite of reduction in hopper height. Consequently, the smallest head loss is obtained for Morel's hopper with a height of 90 *mm*. Among the wall shapes, the greatest increase in head loss is obtained for Sargison's hoppers and similarly the least increase in head loss is obtained for Tapered hoppers as the height is decreased from 150 *mm* to 60 *mm*. This implies that head loss for Sargison's hopper has a strong correlation with hopper height. Similarly, the head loss for Tapered hopper has a weak correlation with hopper height.

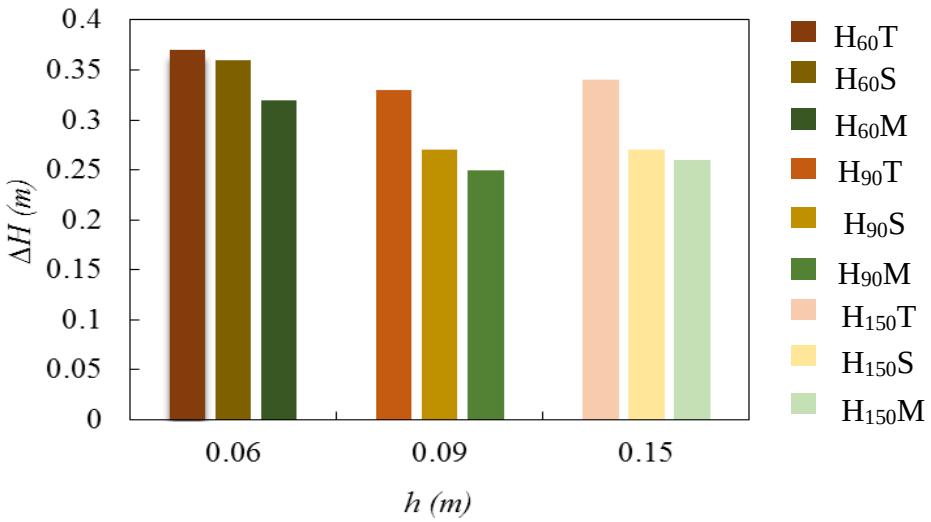

Figure 5.29: Comparison of head loss for the three hopper heights (h = 150 *mm*, 90 *mm* and 60 *mm*) designed using Tapered, Sargison's and Morel's methods.

6 CHAPTER: SUMMARY AND CONCLUSIONS

6.1 Summary

An experimental and numerical study is conducted to investigate the flow characteristics through the Refuge One hopper, to numerically simulate flow through the Refuge One hopper and compare the predictive performance of five different turbulence models, and to optimize the hopper geometry. A high resolution particle image velocimetry system is used to perform detailed velocity measurements within the Refuge One hopper to better understand the flow characteristics. The experiments are conducted at Reynolds numbers based on the maximum exit velocity and exit diameter of the hopper, Re_d = 53,000 and 23,000 to investigate the effects of Reynolds number on the flow characteristics. Numerical simulations of the flow are performed using $k-\varepsilon$, RNG $k-\varepsilon$, $k-\omega$, $k-\omega$ based SST and Reynolds stress models in ANSYS CFX 15.0. For the optimization study of hopper geometry, three different hopper heights, h = 150 *mm*, 90 *mm* and 60 *mm* are selected for Tapered, Sargison's and Morel's wall shapes.

6.2 Conclusions

The major conclusions are summarized as follows

1. The mean flow characteristics, turbulent kinetic energy and Reynolds shear stress through the Refuge One hopper are weakly dependent on the Reynolds numbers investigated in this study.

2. The mean velocity profiles predicted by all the turbulence models through the Refuge One hopper are qualitatively and quantitatively similar, however only $k-\omega$ and $k-\omega$ based SST models captures velocities near the wall. Comparison between the numerical and experimental values demonstrates that the shape of the mean velocity

profiles are reasonably predicted by all the turbulence models. Near the hopper inlet, however, all the turbulence models over predict the streamwise mean velocity and under predict the wall-normal mean velocity.

3. From the optimization study, it is found that hoppers designed with Morel's wall shape performs better compared than hoppers designed with Tapered and Sargison's wall shapes in terms of flow non-uniformity, pressure distribution and head loss.

5. Optimization of hopper geometry also shows that as the hopper height decreases the head loss and flow non-uniformity increase; however the least head loss is obtained for Morel's hopper with height 90 *mm*. The results also show that the difference between the three wall shapes decreases as the hopper height is reduced.

6.3 Future work

It is recommended that experimental study should be conducted for the hopper configuration designed using Morel's equations to confirm the findings of the numerical simulations. Future work should also measure pressure difference through the hopper since this will facilitate comparison of the head losses.

REFERENCES

Abdelhamed, A. S., Yassen, Y. S., & ElSakka, M. M. (2014). Design optimization of three dimensional geometry of wind tunnel contraction. Ain Shams Engineering Journal, 6(1), pp. 281–288.

Ahmed, D. E., & Eljack, E. M. (2014). Optimization of model wind tunnel contraction using CFD. In 10th International Conference on Heat Transfer, Fluid Mechanics and Thermodynamics (pp. 87–92).

Barth, T. J., & Jespersen, D. C. (1989). The design and application of upwind schemes on unstructured meshes. AIAA Paper 89-0366.

Bell, J. H., & Mehta, R. D. (1989). Design and calibration of the mixing layer and wind tunnel.

Boger, D. V. (1987). Viscoelastic flows through contractions. Annual Review of Fluid Mechanics, 19(1), pp. 157–182.

Bouriga, M., Morency, F., & Weiss, J. (2014). Preliminary experimental and numerical investigations of the flow inside a boundary layer wind tunnel. Transactions of Canadian Society For Mechanical Engineering, 38(4), pp. 517–532.

Bullen, P. R., Cheeseman, D. J., & Hussain, L. A. (1996). A study of turbulent flow in pipe contractions. Journal of Process Mechanical Engineering, 210, pp. 171–180.

Bullen, P. R., Cheeseman, D. J., Hussain, L. A., & Ruffell, A. E. (1987). The determination of pipe contraction pressure loss coefficients for incompressible turbulent flow. International Journal of Heat and Fluid Flow, 8(2), pp. 111–118.

Celik, I. (2005). RANS/LES/DES/DNS: The Future Prospects of Turbulence Modeling. Journal of Fluids Engineering, 127(5), pp. 829–830.

Clark, C. E., (Ph.D. thesis). (2010). Design studies in fluid dynamics: I development of a low speed wind tunnel, II hydrodynamics of the exhaust duct of a hydrokinatic turbine. Department of Mechanical and Aerospace Engineering, Carleton University.

Coleman, H. W., & Steele, W. G. (1995). Engineering application of experimental uncertainty analysis. AIAA Journal, 33(10), pp. 1888–1896.

Durst, F., & Loy, T. (1985). Investigations of laminar flow in a pipe with sudden contraction of cross sectional area. Computers & Fluids, 13(1), pp. 15–36.

Fang, F. M. (1997). A design method for contractions with square end sections. Journal of Fluids Engineering, 119, pp. 454–458.

Fang, F. M., Chen, J. C., & Hong, Y. T. (2001). Experimental and analytical evaluation of flow in a square-to-square wind tunnel contraction. Journal of Wind Engineering and Industrial Aerodynamics, 89, pp. 247–262.

Fester, V., Mbiya, B., & Slatter, P. (2008). Energy losses of non-Newtonian fluids in sudden pipe contractions. Chemical Engineering Journal, 145(1), pp. 57–63.

Forliti, D. J., Strykowski, P. J., & Debatin, K. (2000). Bias and precision errors of digital particle image velocimetry. Experiments in Fluids, 28(5), pp. 436–447.

Gardiner, E. J., Raber, M. B., Kuzyk, G. W., Hawkins, R., Simoneau, B. D., Glassford, R., Redkop, T., & Schubert, W., (Underground Research Laboratory). (1993). Operation Tommyknocker test of survival equipment for underground refuge stations. Lac du Bonnet, Manitoba.

Gatski, T. B., & Rumsey, C. L. (2002). Linear and nonlinear eddy viscosity models. Closure strategies for turbulent and transitional flows. In B. Launder & N. Sandham (Eds.), (pp. 10–46). Cambridge university press.

Gnglielmini, G., Lorenzi, A., Muzzio, A., & Sotgia, G. (1986). Two phase flow pressure drops across sudden area contractions pressure and void fraction profiles. In 8th International Heat Transfer Conference (pp. 2361–2366).

Grenier, M., Vergunst, J., Smith, M., Butler, K., Hardcastle, S., & Simoneau, B. (1994). Operation Tommyknocker, phase II - evaluation of the Rimer Alco, RANA-AIR mine refuge system at Falconbridge Ltd., Kidd Creek division. Falconbridge Ltd, Kidd Creek division, Ontario.

Han, Y. O., George, W. K., & Hjarne, J. (2005). Effect of a contraction on turbulence. part I: experiment. AIAA Journal, pp. 1–18.

Hanjalic, K. (1994). Advanced turbulence closure models: a view of current status and future prospects. International Journal of Heat and Fluid Flow, 15(3), pp. 178–203.

Hussain, A. K. M. F., & Ramjee, V. (1976a). Effect of axisymmetric contraction shape on imcompressible turbulent flow. Journal of Fluid Engineering, pp. 58–68.

Hussain, A. K. M. F., & Ramjee, V. (1976b). Influence of the axisymmetric contraction ratio on free stream turbulence. Journal of Fluid Engineering, 98(3), pp. 506–515.

Hussain, L.A., (Ph.D. Thesis). (1990). The experimental and theoretical analysis of pipe contraction flow fields. Department of Mechanical, Aeonautical and Production Engineering, Kingston University.

Hwang, R. R., & Jaw, S. Y. (1998). Second order closure models: their achievements and limitations. In In Proceedings of the National Science Council (pp. 703–722).

Jansen, E. (1966). Two phase pressure loss across abrupt contractions and expansions, steam water mixtures at 600-1400 psia. In International Heat Transfer Conference ASME (pp. 13–25).

Javed, K., & Ali, M. (2014). Design & Construction of subsonic wind tunnel focusing on two dimensional contraction cone profile using sixth order polynomial. In Scientific Cooperations International Workshops on Engineering Branches (pp. 287–296).

Khezzar, L., & Whitelaw, J. H. (1988). Flows thorugh round sudden contractions. In Proceedings of the Institution of Mechanical Engineers, Part C: Mechanical Engineering Science (pp. 295–300).

Launder, B. E., Reece, G. J., & Rodi, W. (1975). Progress in the development of a Reynolds-stress turbulence closure. Journal of Fluid Mechanics, 68(03), pp. 537–566.

Launder, B. E., & Sharma, B. I. (1974). Application of the energy dissipation model of turbulence to the calculation of flow near a spinning disc. Letters in Heat and Mass Transfer, 1(2), pp. 131–137.

Launder, B. E., & Spalding, D. B. (1974). The numerical computation of turbulent flows. Computer Methods in Applied Mechanics and Engineering, 3, pp. 269–289.

Leschziner, M. A. (2006). Modelling turbulent separated flow in the context of aerodynamic applications. Fluid Dynamics Research, 38(2-3), pp. 174–210.

Marshall, B., (The Mining Association of Canada). (2013). Facts and figures of the canadian mining industry.

Mathew, J., (Ph.D. Thesis). (2006). Design, fabrication, and characterization of an anechoic wind tunnel facility. Department of Mechanical and Aerospace Engineering, University of Florida.

Mattos, B., Fico, N. G. C. R., & Girardi, R. M. (2003). Design of ITA ' s research wind tunnel contraction using CFD tools. In 21st Applied Aerodynamics Conference.

Mei, R., Adrian, R. J., & Hanratty, T. J. (1991). Particle dispersion in isotropic turbulence under Stokes drag and Basset force with gravitational settling. J. Fluid Mech., 225, pp. 481–495.

Menter, F. R. (1994). Two equation eddy viscosity turbulence models for engineering applications. AIAA Journal, 32(8), pp. 1598–1605.

Mikhail, M. N. (1979). Optimum design of wind tunnel contractions. AIAA Journal, 17(5), pp. 471–477.

Morel, T. (1975). Comprehensive design of axisymmetric wind tunnel contractions. Journal of Fluids Engineering, 97(2), pp. 225–233.

Morel, T. (1977). Design of two dimensional wind tunnel contractions. Journal of Fluid Engineering, 99(2), pp. 371–379.

Ozalp, C., Pinarbasi, A., Fakilar, M. S., & Sahin, B. (2007). PIV measurements of flow through a sudden contraction. Flow Measurement and Instrumentation, 18(3-4), pp. 121–128.

Pope, S. B. (2000). Turbulent flows. Cambridge university press.

Prasad, A. K., Adrian, R. J., Landreth, C. C., & Offutt, P. W. (1992). Effect of resolution on the speed and accuracy of particle image velocimetry interrogation. Experiments in Fluids, 13(2-3), pp. 105–116.

Prinos, P., & Goulas, A. (1993). Flow characteristics in a pipe with a gradual contraction. Journal of Hydraulic Research, 31, pp. 587–600.

Raffel, M., Willert, C. E., & Kompenhans, J. (1998). Particel image velocimetry: A practical guide. New York: Springer.

Ray, S., Biswas, N., & Roy, P. C. (2012). Investigation of Newtonian fluid flow through a two - dimensional sudden expansion and sudden contraction flow passage. International Journal of Engineering Research and Development, 1(12), pp. 1–9.

Rhie, C. M., & Chow, W. L. (1983). A numerical study of the turbulent flow past an isolated airfoil with trailing edge separation. AIAA Journal, 21(11), pp. 1521–1532.

Rimer Alco North America. (2010). Refuge One Air Centre product sheet. Retrieved January 11, 2015, from http://www.ranacaregroup.com/mine-refuge-systems/products/refuge-one-air-centre/specifications

Roul, M. K., & Dash, S. K. (2008). Two - phase pressure drop caused by sudden contractions in flow areas. In 19th National & 8th ISHMT-ASME Heat and Mass Tranfer Conference.

Sanchez, F. P., Machuca, J. L., Franco, A. T., & Morales, R. E. M. (2010). Experimental and numerical study of turbulent Newtonian flow through an axisymmetric sudden contraction. In 13th Brazilian Congress of Thermal Sciences and Engineering. Uberlandia, Brazil: 13th Brazilian congress of thermal Sciences and Engg.

Sargison, J. E., Walker, G. J., & Rossi, R. (2004). Design and calibration of a wind tunnel with a two dimensional contraction. In 15th Australasian Fluid Mechanics Conference.

Schmidt, J., & Friedel, L. (1977). Two phase pressure drop across sudden contraction in duct areas. International Journal of Multiphase Flow, 23, pp. 283–299.

Smith, R. H., & Wang, C. T. (1944). Contraction cones giving uniform throat speeds. Journal of Aeronautical Sciences, 11, pp. 356–360.

Sousa, P. C., Coelho, P. M., Oliveira, M. S. N., & Alves, M. A. (2011). Effect of the contraction ratio upon viscoelastic fluid flow in three dimensional square - square contractions. Chemical Engineering Science, 66(5), pp. 998–1009.

Szczenioeski, B. (1943). Contraction cone for a wind tunnel. Journal of Aeronautical Sciences, 10, pp. 311–312.

Thwaites, B. (1946). On the design of contractions for wind tunnels. Aeronautical Research Council.

Tsein, H. S. (1943). On the design of the contraction cone for a wind tunnel. Journal of the Aeronautical Sciences, 10, pp. 68–70.

Tulapurkara, E. G. (1980). Studies on Thwaites method for wind tunnel contraction. Aeronautical Journal, 84, pp. 167–169.

Tulapurkara, E. G., & Bhalla, V. V. K. (1988). Experimental investigation of Morel's method for wind tunnel contractions. Journal of Fluids Engineering, 110(1), pp. 45–47.

Uberoi, M. S. (1956). Effect of wind tunnel contraction on free stream turbulence. Journal of Aeronautical Sciences, 23(8), pp. 754–764.

Versteeg, H. K., & Malalasekera, W. (2007). An introduction to computational fluid dynamics the finite volume method. Pearson Education Limited, U.K.

Vrentas, J. S., & Duda, J. L. (1973). Flow of a newtonian fluid thorugh a sudden contraction. Applied Scientific Research, 28, pp. 241–260.

Watmuff, J. (1986). Wind tunnel contraction design. In Proceedings of 9th Australian Fluid Mechanics Conference (pp. 472–475).

Wexler, C., (Ph.D. thesis). (2014). Experimental measurement and computational simulation of the flow in the Queen ' s university. Department of Mechanical and Material Engineering, Queen's University.

Wilcox, D. C. (1986). Multiscale model for turbulent flows. AIAA Journal, 26(11), pp. 1311–1320.

Wilcox, D. C. (1994). Turbulence modeling for CFD. DCW Industries.

Willert, C. E., & Gharib, M. (1991). Digital particle image velocimetry. Experiments in Fluids, 10, pp. 181–193.

Yakhot, V., Orszag, S. A., Thangam, S., Gatski, T. B., & Speziale, C. G. (1992). Development of turbulence models for shear flows by a double expansion technique. Physics of Fluids, 4(7), pp. 1510–1520.

Yassen, Y. E., & Abdelhamed, A. S. (2015). Design of mini wind tunnel based on coanda effect. American Journal of Aerospace Engineering, 2, pp. 31–37.

Yu, Y., Shademan, M., Barron, R. M., & Balachandar, R. (2012). CFD study of effects of geometry variations of flow in a nozzle. Engineering Applicatons of Computational Fluid Mechanics, 6(3), pp. 412–425.